Microscopy, 2022, **71(S1)**, i174–i199
DOI: https://doi.org/10.1093/jmicro/dfab050
Supplement Paper

MICROSCOPY

Advances in ultrahigh-energy resolution EELS: phonons, infrared plasmons and strongly coupled modes

Maureen J Lagos[1,2,*], Isobel C Bicket[2], S Shayan Mousavi M[1] and Gianluigi A Botton[1,3,*]

[1]Department of Materials Science and Engineering, McMaster University, 1280 Main St W, Hamilton, L8S 4L8, ON, Canada
[2]Canadian Centre for Electron Microscopy (CCEM), McMaster University, 1280 Main St W, Hamilton, L8S 4M1, ON, Canada
[3]Canadian Light Source, 44 Innovation Boulevard, Saskatoon, S7N 2V3, SK, Canada
[*]To whom correspondence should be addressed. E-mail: mjlagos@mcmaster.ca (M.J.); E-mail:gbotton@mcmaster.ca (G.A.)
This manuscript is dedicated to the Japanese Society of Microscopy, in recognition of the pioneering work in electron microscopy techniques by Japanese scientists over the last 70 years.

Abstract

Nowadays, sub-50 meV atom-wide electron probes are routinely produced for electron energy loss spectroscopy in transmission electron microscopes due to monochromator technology advances. We review how gradual improvements in energy resolution enabled the study of very low-energy excitations such as lattice phonons, molecular vibrations, infrared plasmons and strongly coupled hybrid modes in nanomaterials. Starting with the theoretical framework needed to treat inelastic electron scattering from phonons in solids, we illustrate contributions in detecting optical surface phonons in photonic structures. We discuss phonon mapping capabilities in real and reciprocal space, and the localized phonon response near nano-/atomic-scale structural features. We also survey the progress of aloof spectroscopy in studying vibrations in organic materials and applications in measuring local temperature and photonic density of states in single nanostructures using phonon scattering. We then turn towards studies on infrared plasmons in metals and semiconductors. Spectroscopy analyses now extend towards probing extremely complex broadband platforms, the effects of defects and nanogaps, and some far-reaching investigations towards uncovering plasmon lifetime and 3D photonic density of states. In doped semiconductors, we review research on the use of the electron probe to correlate local doping concentration and atomic-scale defects with the plasmonic response. Finally, we discuss advances in studying strong coupling phenomena in plasmon–exciton and plasmon–phonon systems. Overall, the wealth of information gained extends our knowledge about nanomaterial properties and elementary excitations, illustrating the powerful capabilities of high-energy resolution scanning transmission electron microscopy–electron energy loss spectrometry.

Key words: Monochromated STEM-EELS, vibrational EELS, phonons, strongly coupled excitations, infrared plasmons

Introduction

The development of new materials with compelling properties represents the bedrock of the most advanced technologies in solid-state transistors, thermal devices, infrared imaging detectors, biosensors, etc. While advances in materials are rapidly evolving in different areas, new instruments and methodologies for measuring unique material properties are still under development. In the field of (scanning) transmission electron microscopy ((S)TEM), the need for structural and chemical analyses of materials over a wide range of length scales drives characterization tool development. For instance, the development of aberration correctors for electron microscopes has enabled sub-Ångstrom structural characterization [1–7], pushed even further by ptychographic reconstruction methods [8,9]. Parallel electron energy loss spectrometers and energy filters for chemical imaging revolutionized chemical analysis with remarkable spatial resolution [10–12], while ultra-sensitive detectors for protein imaging, diffraction pattern detection and low-noise spectroscopy provide opportunities to study sensitive materials [13]. These developments in electron microscopy have extended our understanding of the physical and chemical properties of (nano)materials.

Despite those instrumental breakthroughs, the development of electron spectroscopic instrumentation for the study of mid-infrared (MIR) excitations and electronic structure with both high spatial and energy resolution is still in progress. This challenge involves the reduction of the intrinsic energy width of the emitted electrons (typically hundreds of meV) to a few meV (Fig. 1a), while keeping a nanometre/Ångstrom-wide electron probe with enough current (> 5 pA). The benefits of monochromatic conditions are 2-fold: access to the IR range due to strong suppression of the zero-loss peak (ZLP) tails and the ability to resolve electronic transitions. Substantial efforts towards monochromator development in STEMs bring the electron energy loss spectroscopy (EELS) community gradually closer to the goal of matching the energy resolution (sub-1 meV) available on high-energy resolution EELS (HR-EELS) setups operating in the reflected geometry [14,15].

Current energy resolution improvements in STEMs have already opened the doors for high spatial resolution investigations of elementary excitations such as lattice phonons, molecular vibrations, infrared plasmons, hybrid modes, excitons, etc. A fuller understanding of the behaviour of those excitations and electronic properties at/near structural

Received 30 September 2021; Revised 20 November 2021; Editorial Decision 22 November 2021; Accepted 26 January 2022

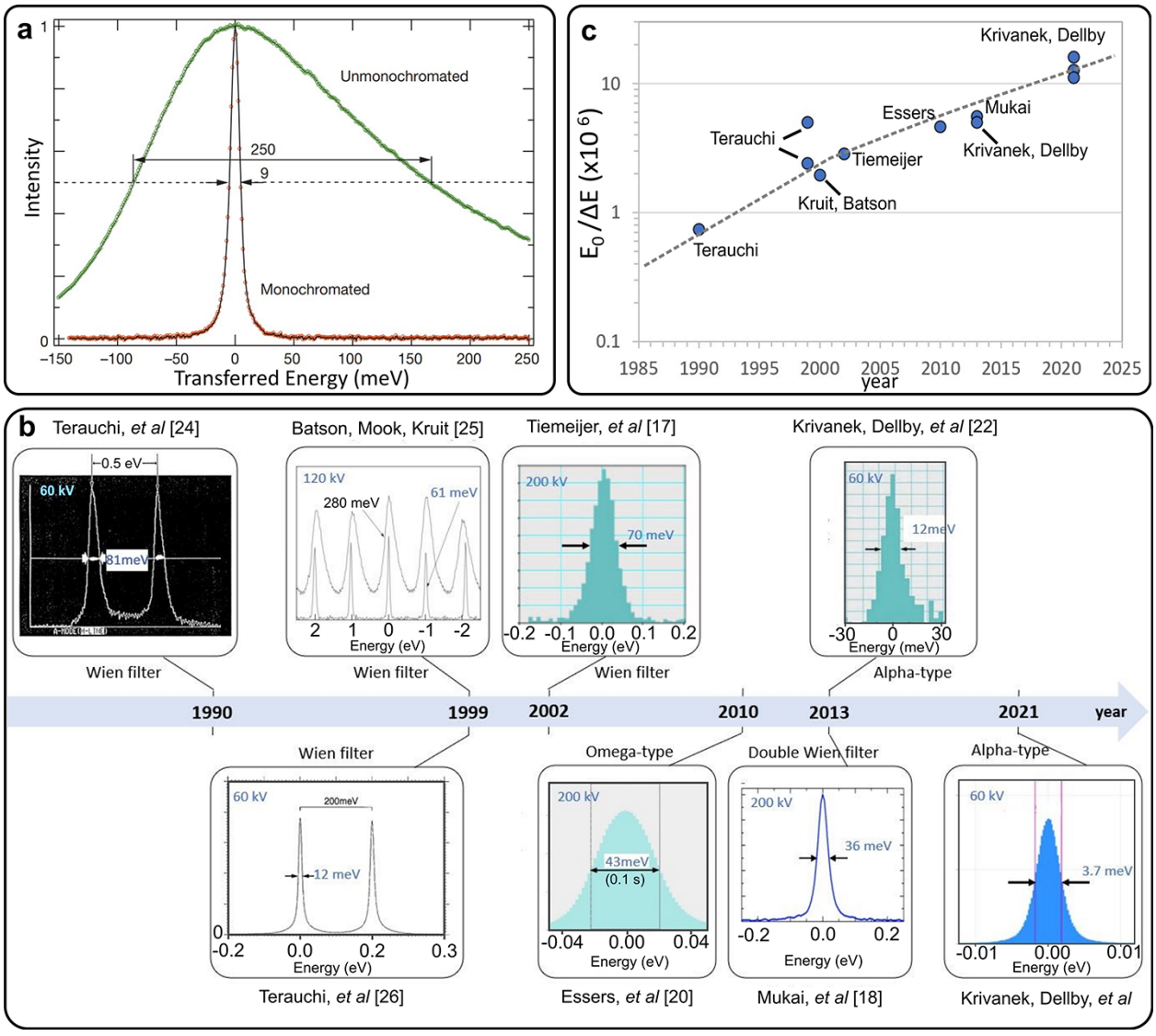

Fig. 1. Evolution of high-energy resolution STEM-EELS. (a) ZLP spectra for an unmonochromated and a monochromated beam at 60 kV. Energy resolution of 9 meV is achieved using an alpha-type magnetic monochromator. (Adapted with permission from Springer Nature Customer Service Centre GmbH: Nature [27], © 2014.) (b) Timeline of energy resolution improvements highlighting landmark results over the last thirty years. (Top row. Terauchi: adapted with permission [24]. Batson, Mook, and Kruit: © 2000 from [25], adapted with permission of Taylor and Francis Group, LLC, a division of Informa plc. Tiemeijer *et al.*: [17], adapted with permission. Krivanek, Dellby *et al.*: adapted from [22], by permission of the Japanese Society of Microscopy. *Bottom row*. Terauchi *et al.*: adapted from [26], © 1999, the Royal Microscopical Society. Essers *et al.*: adapted from [20], © 2010, with permission from Elsevier. Mukai *et al.*: adapted from [18], with permission from Elsevier. The 2021 ZLP was recently obtained from the CCEM monochromated microscope.) (c) Plot of the ratio between the electron kinetic energy and energy resolution as a function of time. Figure of merit (FOM) values were derived from information presented in b.

features (e.g. defects and interfaces) will push the frontiers of knowledge in fields such as superconductivity, optoelectronics, photonics, phononics, biomedicine, etc. Specifically, studying phonon-based physical and chemical properties in single nanostructures or near nanoscale structural features requires the use of local probes with high spatial sensitivity. The study of IR surface plasmon excitations benefits from the use of nanoscale probes in uncovering the fundamentals of how shape, size, and material affect the localization and behaviour of both optically bright and dark surface plasmon modes. In analogous manner, spatially resolved EELS studies of hybrid excitations can unlock new physics of strong (extreme) coupling phenomena, including the detection of dark polaritons in hybrid systems. Progress in the arena of high-energy resolution STEM-EELS applied to phonons, infrared plasmons, and hybrid coupled modes is just beginning, promising a bright future for the study of advanced material properties. Here we review the advancement of high-energy resolution monochromators in STEMs and current progress in the study of phonon/vibrational excitations, infrared plasmons, and strongly coupled modes using electron probes.

Progress on high-energy resolution STEM-EELS

Several monochromators have been implemented in STEMs, including four different primary configurations – the single Wien filter [16,17], the double Wien Filter [18], the

omega-shaped electrostatic monochromator [19,20], and the alpha-type magnetic monochromator [21,22]. We refer the reader to the review on monochromators by Kimoto [23] and references therein to obtain an in-depth description of monochromators implemented in TEM/STEMs.

Figure 1b presents an overview of the progress on energy resolution in STEM-EELS over the last thirty years, highlighting some landmark results obtained using different monochromator models. In this context, the energy resolution is traditionally defined as the full width at half maximum of the ZL spectrum acquired in vacuum. Pioneering work by Terauchi *et al.* [24] in 1991 showed a drastic improvement down to 80 meV at 60 kV using Wien filters in a monochromator-analyser configuration, but with limited beam current imposed by the usage of a thermionic source. In the late nineties, Batson, Mook, and Kruit [25] implemented a fringe-field Wien filter in a STEM equipped with a field-emission source, demonstrating 61 meV at 120 kV. At the same time, the energy resolution barrier was again pushed down to 12 meV at 60 kV by Terauchi and coworkers through the use of better retarding Wien filters and a Schottky-type electron gun [26]. They reported some initial studies on the electronic structure properties of superconductors and dielectrics in real and momentum space, highlighting the potential of STEM-EELS using a nanometre-sized electron probe.

Tiemeijer *et al.* proposed [16] and built [17] a single Wien filter monochromator around the turn of the century, showing energy resolution of 70 meV at 200 kV, with better performance at lower voltages. This improvement resulted in reductions to the ZLP tails, allowing the study of plasmonic and electronic properties in the visible and NIR range. For instance, multiple localized surface plasmon resonances (LSPRs) down to 170 meV were detected in silver nanowires (NWs) [28]. As a matter of fact, high-energy resolution spectroscopy studies have led to significant contributions from the EELS community to the areas of nanophotonics and materials science (see Spectroscopy of Plasmons).

Subsequently, other monochromators were designed and incorporated into STEMs. In 2010, Essers *et al.* [20] reported on the development of an omega-type monochromator operating in tandem with a MANDOLINE analyser, which further pushed the limits of energy resolution to 40 meV at 200 kV. In 2012, Mukai *et al.* [18] reported the use of a double Wien filter to reduce the ZLP width down to 36 and 26 meV at 200 and 80 kV, respectively. Krivanek and coworkers [22] designed and built an alpha-type monochromator, which delivered 12 meV at 60 kV, matching the energy resolution obtained by Terauchi in 1999, but with enhanced stability. Instrument instabilities lead to ZLP broadening, typically observed on measurements with large acquisition times. These instrumental advances allowed the detection of vibrational modes at the nanoscale; in 2014, Miyata *et al.* [29] and Krivanek *et al.* [27] independently reported the first vibrational spectra from nanostructures using STEM-EELS.

Although the energy resolution is considered as the typical FOM, it is known that the energy resolution depends on factors such as accelerating voltage, probe convergence angle, beam current, etc. suggesting the use of other FOM expressions that include such dependence in order to characterize the overall optical quality of monochromators and allow comparison between them. Inspired by the resolving power used to characterize spectrometers and analysers in HR-EELS [30], we have computed a unitless quantity given by the ratio between the accelerating energy (E_0) and energy resolution (ΔE) (Fig. 1c) to highlight the gradual enhancement of performance over the last thirty years. Furthermore, it has been recognized by the EELS community that the decay of the ZLP tails also represents an important parameter to consider when assessing an instrument's ability to detect excitations or electronic transitions (e.g. bandgaps and defect states) near the ZLP [31], since strong tails tend to hinder the detection of weak inelastic scattering signal. Values of FW at 1% and below the ZLP intensity are useful references [18].

Nowadays, different types of monochromators work in tandem with better spectrometers and detectors and overall performance has improved gradually over the years. One example is illustrated by improvements to the alpha-type monochromator since 2013, which can now reach 3.7 and 7.9 meV at 60 and 100 kV, respectively (Fig. 1b). This progress represents a remarkable achievement, offering the EELS community similar instrumental capabilities as those in HR-EELS [32], but with the advantage of using a nanometre/Ångstrom-sized monochromatic beam for spectroscopy studies. Furthermore, STEMs can also operate under different alignment settings, permitting both spatially resolved and momentum-resolved acquisitions to provide information about materials in real and reciprocal space, respectively.

Spectroscopy of phonons

Phonons represent one of the most fundamental excitations that a solid can sustain. Both surface and bulk phonon modes can co-exist on a finite-size structure and unveiling their behaviour underpins the understanding of numerous physical processes, including heat transport, phonon-driven superconductivity, light–matter interaction, etc. Bulk phonon studies are dominated by neutron, IR light and x-ray spectroscopies, while the study of surface phonons usually requires the use of surface-sensitive techniques, such as Raman spectroscopy, HR-EELS, etc., but studying phonon-based properties in single nanostructures or near nanoscale structural features benefits from the use of nanoscale probes. This section describes the progress in the new field of EELS applied to the study of vibrational modes in small volumes of matter, denominated vibrational EELS (vibEELS). We present a summary of progress in theoretical models of inelastic electron scattering from lattice phonons; excitation of surface phonon modes; phonon mapping in real space and momentum space; localized phonon scattering in solids and structural features; the study of vibrational modes in organic materials; and the use of vibEELS to measure physical properties such as temperature and phonon polariton density of states.

Inelastic electron scattering from phonons in solids

Theoretical models of the inelastic electron scattering from lattice phonons in solids date back to the works by Glauber and Van Hove [33,34] on density–density correlation functions. Since then, several theoretical models of the inelastic scattering by fast electrons were developed following similar quantum treatments relying on the Born–Oppenheimer approximation [35–38] and including some of the key ingredients associated with electron scattering in crystalline samples,

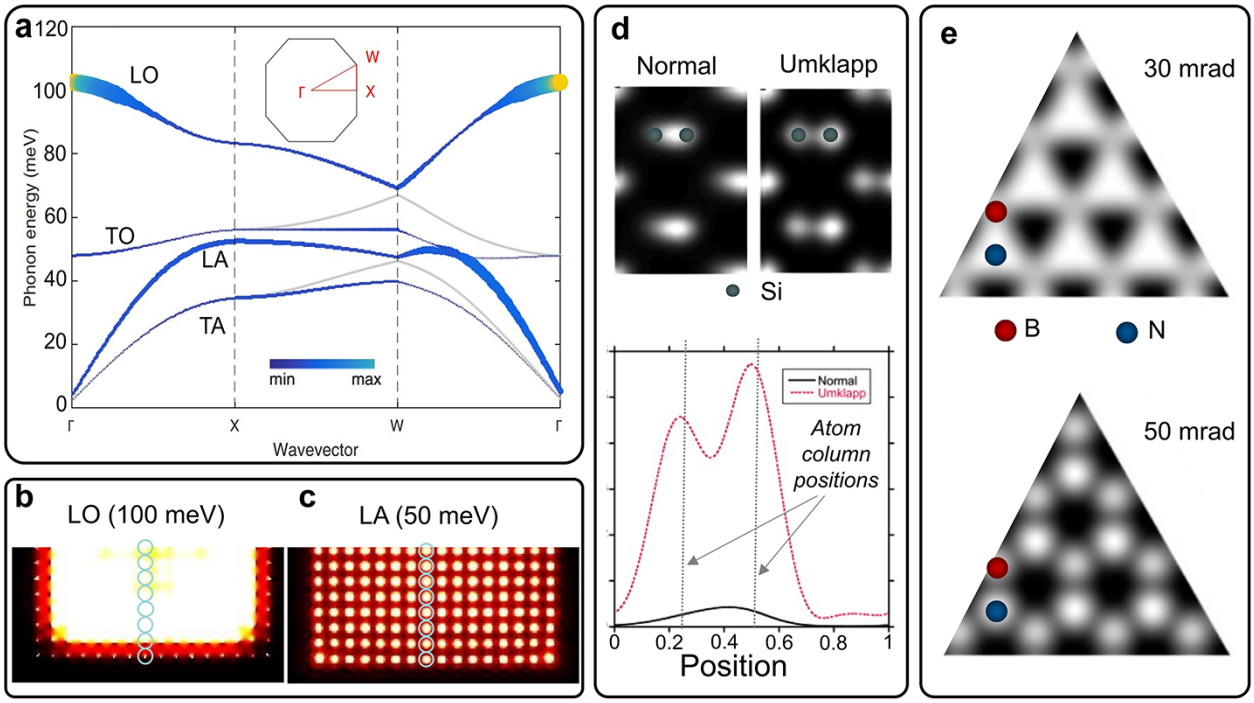

Fig. 2. Theoretical formulation of inelastic electron scattering from phonons. (a) Coupling constant strength for excitation of bulk phonon modes of MgO. Grey curve indicates phonon dispersion curves and overlaid linewidth indicates the coupling strength. (b) EELS scattering maps of longitudinal optical (LO) phonon at the gamma point (100 meV) showing delocalized scattering and (c) the bulk longitudinal acoustic (LA) phonon mode at the BZ edge (50 meV) showing atom-level localization (circles indicate the atomic columns in MgO). (Adapted figures with permission from [37], © 2018 by the American Physical Society.) (d) Normal and Umklapp scattering contributions from a phonon peak between 35-45 meV, (top) simulated image of Si dumbbells and (bottom) line profiles across the image showing the relative contributions from normal and Umklapp components. (Adapted from [43], with permission from Elsevier.) (e) Calculated vibEELS images of monolayer *h*-BN with 30 and 50 mrad EELS collection semiangles. (Adapted figure with permission from [40], © 2017 by the American Physical Society.)

such as multiple elastic interactions among different beams and dynamical diffraction [39–43].

The common denominator among all those models is that the scattering cross-sections can be described as the product of two main terms: the probe component (Fourier transform of the Coulomb potential of the travelling electron) and the dynamical form factor (the spectrum of excitations in the solid in the absence of the probe). The Fourier term is inversely proportional to the scattering wavevector ($\mathbf{q}^2$), which describes the gradual decay of the inelastic scattering signal from the Brillouin zone (BZ) centre towards the BZ boundaries. The dynamical form factor ($S(\mathbf{q},\omega)$) includes the transition element matrix, which offers a description of the excitations of vibrations in bulk matter in terms of the dipole ($\Delta\mathbf{q} \to 0$) and impact ($\Delta\mathbf{q} \gg 0$) scattering contributions and is subject to scattering (sum) selection rules imposed by the conservation of particles within the system [44]. The scattering cross-section also includes the Bose–Einstein phonon population terms (n) that appear naturally from the quantum treatment of scattering at a certain temperature.

The transition elements embedded in $S(\mathbf{q},\omega)$ can be represented by a combination of dot product terms between the polarization of the oscillating atoms and the transferred wavevector ($\mathbf{e}\cdot\Delta\mathbf{q}$), weighted by different terms. These summed contributions describe the coupling between a fast electron and individual phonon modes and can be reduced to an $\mathbf{e}\cdot\Delta\mathbf{q}$ term in the dipole limit ($\Delta\mathbf{q} \to 0$), facilitating the interpretation of scattering data [36]. An instructive example of the coupling is illustrated in Fig. 2a, which shows the coupling strength constant for the excitation of bulk phonon modes of a MgO crystal using 60 kV electrons [37]. At the centre of the BZ (Γ point) only small amounts of momentum transfer are needed for the electron to excite phonons and the electron beam couples more effectively to longitudinal modes than transversal modes. However, at the boundary of the first BZ, large momentum transfers are required and simulations reveal that the coupling is efficient for both longitudinal and transversal short-wavelength modes [37,43]. Interestingly, Hohenester *et al.* showed that, for electron beam positions close to atomic columns, the coupling strength increases for modes near the BZ boundary but remains unchanged for modes at the BZ centre, suggesting spatially dependent scattering behaviour. Experimental measurements of the coupling strength can be obtained using nanometre-sized probes and off-axis collection geometries [45] or angle-resolved spectroscopy settings [46].

Dipole and impact scattering contributions exhibit different degrees of Coulomb delocalization, with the dipole component ($\Delta\mathbf{q} \to 0$) being more delocalized [47], as exemplified by the map of the LO phonon mode at the Γ-point of MgO in Fig. 2b. In this particular example, the EELS signal is nearly uniformly spread within the internal region of the MgO nanocrystal, unaffected by proximity to an atomic column. This behaviour is primarily due to surrounding long-range contributions from the in-phase oscillatory electric dipoles associated with this long-wavelength mode.

The large impact scattering signal ($\mathbf{q} \gg 0$) is less delocalized. Pioneering work by Rez in 1993 [48] suggested

that inelastic scattering from phonons in gold crystals could include an atomic resolution component involving a large momentum transfer. Later, several theoretical models developed by other researchers described atomically localized inelastic scattering behaviour from lattice phonons in different materials (Si, BN and MgO) [37,39,40,42]. Figure 2c illustrates highly localized signal from the LA phonon mode at/near the BZ boundary in an MgO nanocrystal. In contrast to the map for the LO mode (Fig. 2b), scattering from LA modes involves large momentum transfers and can be localized to atomic columns. In this case, out-of-phase ion motion of these short-wavelength modes cancels out contributions from the region surrounding the electron beam path, allowing the interaction between the fast electron and the closest atomic column to dominate.

More recently, Rez *et al.* [43] shed light onto the formation of impact scattering signal by showing the importance of Umklapp processes (phonon excitation that results in scattering from one BZ to another) over normal processes (scattering occurring within the first BZ). As observed in Fig. 2d, the Umklapp contribution dominates the scattering modulation within lattice distances. Material thickness can naturally affect the scattering intensity due to dynamical diffraction effects playing a role in the modulation of the scattering. Moreover, the localization of phonon scattering signal from a one-atom-thick BN layer was predicted by Dwyer [40], showing that large amounts of momentum transfer ($\Delta\mathbf{q} \gg 0$) are required to build higher scattering localization around atomic positions (Fig. 2e) and suggesting the use of large-angle acquisition conditions. This reveals the importance of collection conditions in the modulation of scattering by phonons and demonstrates that localized scattering could be built from a single atomic layer, in which contributions from surrounding oscillating atoms cancel out laterally within an atomic plane. The section on localized phonon scattering will review several recent experiments studying the regime of impact scattering.

The dielectric theory developed by Fermi to describe electron scattering from phonons is completely equivalent to the theoretical treatments mentioned above. So far, the dielectric formalism has been successfully applied to explain the surface and bulk phonon response of any finite structure in the long-wavelength limit ($\mathbf{q} \to 0$). Dielectric waves such as plasmons and phonons share many similarities and the knowledge derived from the excitation of bulk, surface and interface plasmons using EELS has been translated into the study of vibrational modes [14,49]. In this context, the excitation of Fuchs–Kliewer (FK) surface phonon modes can be predicted in 2D films [50], and polaritonic and non-polaritonic modes can be identified as possible loss channels in Si/SiO_2 interfaces [51,52].

Another scenario to probe excitations within the dipole approximation is the aloof excitation of surface phonon modes because only small wavevectors are transferred during the scattering ($\sim 10^{-3}$ Å^{-1}). For aloof excitation, the scattering signal falls gradually from an object edge following a decay described by a modified Bessel function of the second kind (K_0), demonstrated experimentally in Refs [27,53,54], which also showed that surface phonons can be detected at larger impact parameters than surface plasmons. For instance, aloof surface phonon signal from amorphous carbon films was detected for electrons travelling with an impact parameter of up to 1 μm [55]. Furthermore, the Coulomb delocalization length of the dipole scattering can be estimated using Heisenberg's principle [47]. In this case, a delocalization distance of about 100 nm is derived for 130 meV surface vibrations probed at 60 kV. Aloof spectroscopy brings important advantages in probing beam-sensitive materials (see the section on the vibrational response of beam-sensitive materials) [56].

The use of the dielectric formulation to describe bulk phonon scattering behaviour beyond the BZ centre has so far been limited due to a lack of information about the dielectric function in the short-wavelength limit ($\mathbf{q} \gg 0$) [37]. Also, while the dielectric theory can predict an energy loss event, it cannot describe an energy gain event during an inelastic scattering process. The development of theoretical models to describe the inelastic electron scattering from phonons or vibrational modes in nanoscale structural features plays an important role in the progress of this field. More complex systems such as heterostructure interfaces, molecular systems or proteins bring additional challenges, requiring reliable calculations of the dielectric function or wavevector-dependent phonon frequencies, in combination with realistic theories of electron scattering.

Optical surface phonon excitations

Finite-size structures can sustain both surface and bulk phonon modes. Optical surface phonon modes remain confined within the reststrahlen band (RB) of the material: the spectral region between the transverse optical (TO) and LO modes. Substantial literature on surface phonons in objects of different geometries is already available [57,58], and we limit ourselves to presenting a description of surface excitations in nano- to micro-sized structures, including isotropic and anisotropic thin films, finite slabs, nanoparticles and film–particle composite systems.

Thin films can support surface phonon polariton (SPhP) modes, analogously to their surface plasmon polariton (SPP) counterparts [58]. In an isotropic film, SPhP modes adopt two charge configurations due to the interaction of electromagnetic fields on each surface. They exhibit symmetric and anti-symmetric charge distributions with respect to a bisector plane parallel to the film surface, with most of the dipole currents lying parallel or perpendicular to the film, respectively. The dispersion of these polaritons within the RB is dictated by the film thickness.

Those polaritonic modes were predicted by FK [59] and were initially studied via HR-EELS in the reflection geometry using micrometre-size probes, primarily exciting anti-symmetric FK modes. In the transmission geometry, the symmetric FK modes of the film are predominantly excited, as revealed by computations of the second differential scattering probability, shown in Fig. 3a [50]. Oscillating dipoles produce signal involving scattered electrons of a few microradians, which represents a small fraction (1/1000) of the BZ adjacent to the Γ-point. This dipole signal is usually delocalized over tens of nanometres in the specimen. Lagos *et al.* probed silica thin films in transmission mode (Fig. 3b), showing that two main resonances (55 and 135 meV), with energy dependence on the film thickness, appear due to the existence of two RBs. Each resonance is generated due to anti-symmetric FK modes, as predicted by the dielectric model (Fig. 3a).

SPhPs were also observed in nanostructures of anisotropic materials, in which the dielectric response is dependent on the polariton propagation direction. Several groups have reported

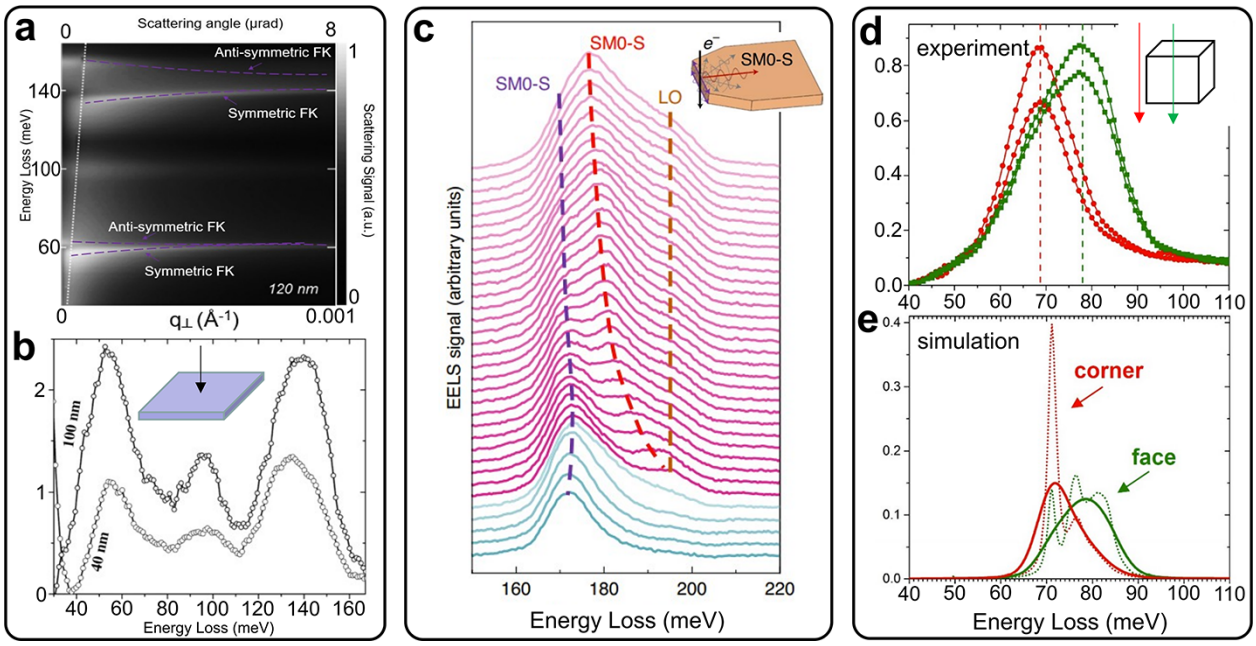

Fig. 3. Surface optical phonons. (a) Calculated double differential scattering probability from SPhPs in a 120-nm *a*-SiO_2 slab, exhibiting two RBs, both supporting symmetric and anti-symmetric FK modes and (b) experimental vibEELS spectra for 40- and 100-nm-thick *a*-SiO_2 slabs, revealing three main resonances. (From [50], by permission of the Japanese Society of Microscopy.) (c) Experimental vibEELS spectra acquired in a line scan across a vacuum–hexagonal boron nitride (*h*-BN) interface (magenta: through the *h*-BN flake, blue: aloof excitation). (Adapted with permission from Springer Nature Customer Service Center GmbH: Springer Nature [60], © 2021.) (d) Experimental vibEELS spectra acquired in aloof configuration, exciting the corner (red circles) and face (green square) modes in an MgO cube oriented along the [001] direction and (e) simulated vibEELS spectra (dotted lines) for an MgO cube under the same excitation conditions as (d), convolved with a 10-meV Gaussian function (solid lines) representing the ZLP. (Adapted with permission from Springer Nature Customer Service Centre GmbH: [61], © 2017.)

on the observation of hyperbolic polaritons in *h*-BN structures, including thin films, truncated slabs and atom-thick layers. Batson used Kroger's equations for dielectric waves [62] to describe the excitation of SPhP in thin *h*-BN films [63], while Egerton *et al.* addressed the lateral and depth resolution of dipole signal from thin films [64]. Govyadinov *et al.* [65] extended the modelling to truncated *h*-BN slabs using finite element methods and revealed that the electron probe excites hyperbolic SPhP propagating along the flake edges, bringing important physical insight to the data interpretation of finite structures. Figure 3c shows typical spatially resolved EELS spectra across a slab–vacuum interface. In aloof geometry, the fast electron primarily excites hyperbolic SPhP modes, whereas in an intersecting geometry, several guided modes are excited due to reflection of those propagating polaritons within the slab, including the LO mode. More recently, Li *et al.* [60] analysed the polaritonic response of a one-atom-thick *h*-BN layer, demonstrating the excitation of highly confined hyperbolic SPhPs. Understanding the behaviour of SPhPs is essential to the development of photonic devices that capitalize on light–matter interaction in the IR range.

Particles sustain localized surface phonon resonances [57], and their phononic dielectric response is dictated by both geometry (shape and size) and composition. For instance, a cube exhibits a large variety of optical phonon excitations due to its unique geometry and symmetry, as predicted by Wallis and Fuchs [66,67]. Lagos *et al.* studied the phononic response of a single MgO nanocube [61] by moving the electron probe to different aloof locations (Fig. 3d). The formation of broad EELS peaks is due to contributions from three narrower resonances (face, edge and corner), as revealed by theoretical simulations (Fig. 3e). The shape of those EELS peaks can also be modified by changing the impact parameter with respective to the cube edge or by probing the cube in different orientations [50,61].

In aloof geometry, bulk phonon modes cannot be efficiently excited (Fig 3c) mainly due to the screening from induced surface charges on the external field of the swift electron. However, Radtke *et al.* [68] reported on the vibrational response of anisotropic $B_{12}P_2$ microparticles, observing several EELS resonances in a spectral range where the calculated dielectric function remains positive and interpreting these as bulk optical phonon excitations. Scattering variations were also detected for $B_{12}P_2$ microparticles oriented along different directions with respect to the beam trajectory, highlighting the directional nature of the dipole mechanism. These variations are imposed by the anisotropy of the material and not only by crystal orientation.

Interactions between surface phonon modes in different structures have been studied theoretically, considering modes in thin film–nanoparticle composite systems. Considering two finite structures (a thin slab and a cube), both phonon mode mixing [49] and transparency behaviour [50] were predicted. Recently, Beutler *et al.* [69] addressed the case of infinite films interacting with single nanospheres, analysing scenarios of strong mode mixing in composite systems and observing that hybridization between FK and Fröhlich modes occurs for certain dimensions of the main constituents. These results bring important physical insights into EELS data interpretation and the quantification of material properties (more detail in the section on nanoscale properties).

Nanoscale phonon mapping in real and reciprocal space

Real space mapping is a well-established methodology to determine the spatial distribution of the scattering signal measured from a nano-/atomic-scale structural feature in nanomaterials. The scattering modulation can reveal important information about the elementary excitations present or the chemical composition of the material under analysis. Real-space imaging is central to the design, synthesis and understanding of functional materials, and its application to a large variety of structural features (e.g. defects and interfaces) is of significant importance to research advances in the fields of materials science, photonics and quantum materials.

By rastering the probe across a nanostructure and collecting the scattered electrons over a circular region in reciprocal space, a phonon scattering map of the nanostructure is obtained. Figure 4a shows spatially resolved maps of phonon EELS scattering acquired on the edge of a 150-nm nanocube [61]. A large variety of spatial distribution patterns associated with each excited surface and bulk phonon mode are visible, including corner (70 meV) and face (77 meV) surface resonances. The same approach has also been used to map out optical surface phonon modes in micrometre-long structures, such as ZnO NWs [70]. These examples reveal that IR polaritons can be supported by structures ranging between nanometre and micrometre scales. Furthermore, the scattering signal from surface phonons measured via EELS experiments is linked to the local density of electromagnetic states (LEMDOS) of the structure, a quantity of paramount importance in photonics [49] (more detail in the section on nanoscale properties).

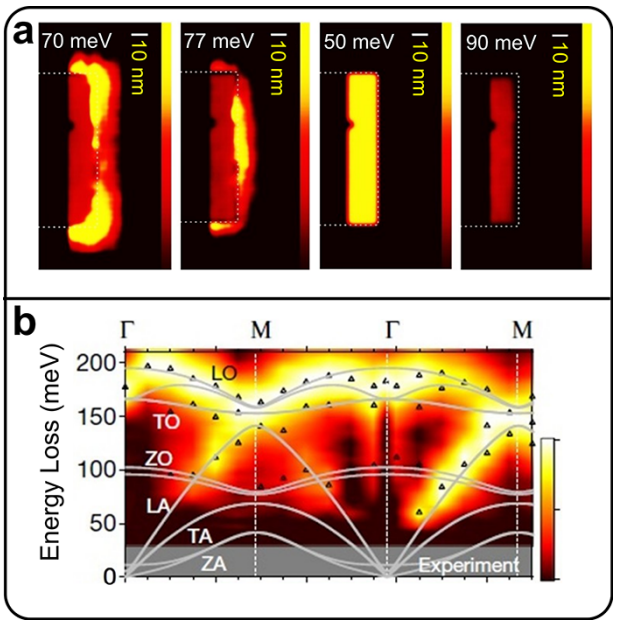

Fig. 4. (a) Experimental vibEELS maps of corner (70 meV) and face (77 meV) SPhP modes, and two bulk phonon excitations (LA: 50 meV, LO: 90 meV). (Adapted with permission from Springer Nature Customer Service Centre GmbH: [61], © 2017.) (b) Experimental momentum-resolved EELS map of phonon modes in *h*-BN, with simulated phonon dispersion curves overlaid as solid lines. (Adapted with permission from Springer Nature Customer Service Centre GmbH: [46], © 2019.)

Bulk acoustic and optical phonon scattering can be also imaged when fast electrons intersect the cube (Fig. 4a); scattering probabilities for these modes are dictated by selection rules. The LO (90 meV) signal remains uniform across the nanocube and decays towards the cube edge, due to a competition between bulk and surface contributions: a process strictly linked to the begrenzung effect. Spatially resolved maps for LA (50 meV) and TA (not shown) modes show stronger signal than the optical modes.

Phonons can also be mapped in reciprocal space using angle-resolved spectroscopy, a methodology used in the past to study the dispersion of plasmon [62] and core-loss transitions [71]. In this case, instead of collecting signal over a large circular area, a slot aperture is employed to select a particular scattering direction in the diffraction plane. Figure 4b shows a reciprocal space mapping of a *h*-BN thin crystal [46]. In this ω-**q** map, not all the phonon modes within the first BZ are excited; coupling is weak to some of the transverse modes, as discussed earlier (see section on inelastic scattering). The ability to access information in reciprocal space is similar to angle-resolved photoemission spectroscopy (ARPES) studies, highlighting the use of vibEELS as a technique to study condensed-matter systems with unprecedented spatial resolution. Progress along this direction is illustrated by phonon mapping in momentum space across a multiwall BN nanotube ($\sim$100 nm in diameter) [72]. The cylindrical geometry changes the orientation of the BN plane from the centre towards the edge, allowing the identification of at least three regions with different phonon dispersions, within a 50-nm region. vibEELS signal near the BZ boundaries and higher-order BZs gets weaker because the inelastic scattering cross-section decays as a function of scattering wavevector, calling for the use of more sensitive detectors to access information beyond the first BZ. Recent advances in direct electron detection cameras [73] have enabled the faster acquisition of scattering signal without readout noise, significantly reducing the acquisition time of maps from hours (Fig. 4) to a few minutes.

Localized phonon scattering signal from bulk crystals, defects and atom-sized systems

Bulk

Atom-wide spatially resolved electron probes are useful for studying the degree of localization of impact scattering in crystalline solids. Over the last four years, two experimental approaches were used to detect localized phonon scattering signal: off-axis and on-axis acquisition geometry conditions.

Off-axis configurations were initially used to collect highly localized scattering signal by Dwyer *et al.* [74], who obtained about 1 nm spatial resolution at the edge of thin BN flakes. The spatial sensitivity limitation was probably due to the strong delocalized dipole signal from polaritonic modes, hindering impact scattering signal detection. Later, a similar off-axis approach was also used by Hage *et al.* [75] to detect vibrational scattering variation on the same system, producing energy-filtered maps which displayed intensity variations at the atomic level. Interestingly, the extracted vibrational signal showed the same modulation as the coherent elastic scattering signal, which added additional complexity to the interpretation of atomic-resolution vibrational signal, preventing unambiguous proof of atom-level localization of phonon scattering. Experiments with different collection conditions can

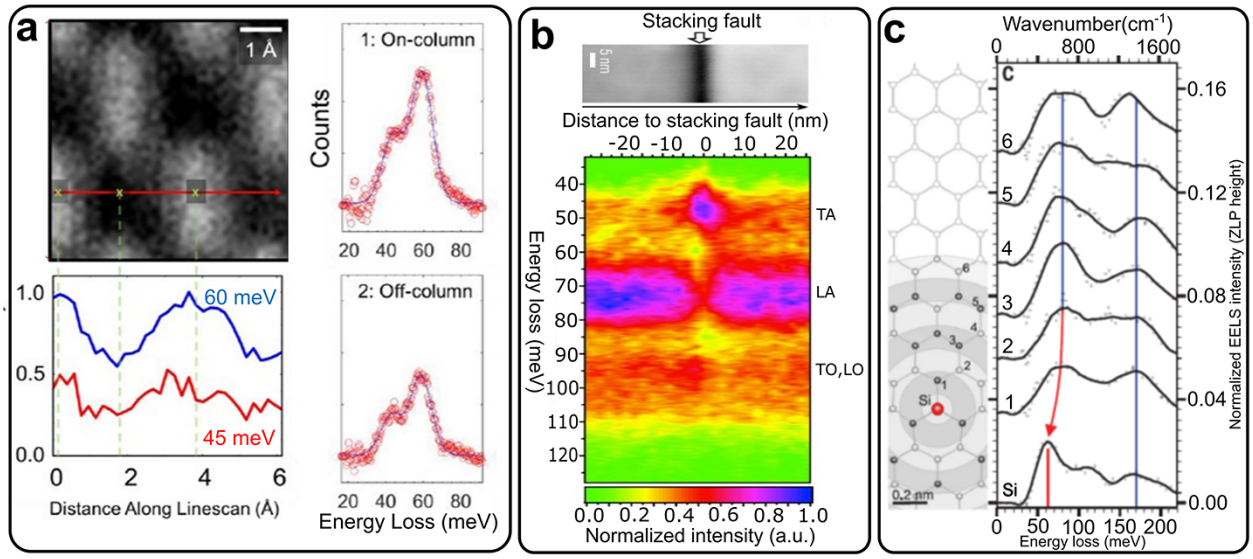

Fig. 5. Highly localized phonon scattering in structural features. (a) Top left: Atomic-resolution annular dark-field image of Si along the [$\bar{1}$10] orientation; bottom left: intensity variation for high (blue) and low (red) energy acoustic phonon peaks visible on the right; right: on- and off-column EEL spectra, revealing an intensity increase over the Si dumbbells. (Adapted with permission from Springer Nature Customer Service Centre GmbH: [77], © 2019.) (b) Top: Annular dark-field (ADF)-STEM image of a stacking fault in SiC; bottom: line profile across the stacking fault of angle-resolved vibEELS spectra at the X point of the BZ. (Adapted with permission from Springer Nature Customer Service Centre GmbH: [79], © 2021.) (c) Left: schematic of a single substitutional Si atom in a graphene lattice; right: v-EEL spectra acquired at locations labelled in the lattice schematic, revealing the localization of the phonon scattering peak near the Si impurity atom. (From [81]. Adapted with permission from AAAS.)

benefit the evaluation of changes of the elastic component collected through the EELS aperture and help to disentangle the elastic signal from the phonon signal. Also, deconvolution methodologies to remove elastic contributions from phonon scattering signal can be useful, similar to those utilized to treat plasmon scattering [76].

On-axis geometry was proposed for conditions in which specific vibrational modes can be excited exclusively by impact scattering. This condition is very useful for probing crystals with dispersive phonon branches that flatten out near or at the BZ boundary, typically producing a high phonon DOS (Fig. 2a). This combination of collection geometry and phonon dispersion behaviour usually produces strong EELS resonances, as shown in covalent and polar materials, such as Si and MgO, respectively. Venkatraman *et al.* [77] demonstrated scattering enhancement around atomic columns in a thin Si crystal, revealing a drastic suppression of about 50% of the phonon scattering signal (60 and 45 meV) for probe positions between columns compared to on-column (Fig. 5a). This highly localized signal has been attributed to the excitation of short-wavelength BZ boundary phonons that underwent Umklapp processes during scattering events [43]. Simulations comparing contributions from normal and Umklapp processes clearly revealed strong scattering contributions from higher-order zones into the first BZ (Fig. 2d).

Planar defects

Electron probes are convenient tools to analyse nanometre structural features such as defects, interfaces, impurities and vacancies. Planar defects affect a crystal's translational symmetry, leading to changes in the bulk phonon properties and new vibrational modes [78]. Yan *et al.* [79] explored the local vibrational response of a stacking fault (SF) in a SiC crystal, finding scattering variations within the optical and acoustic bands at different collection conditions. Off-axis acquisition at high-symmetry points in the diffraction plane show changes in the acoustic phonon signal within the SF region relative to the defect-free region. Figure 5b shows a 2D map of acoustic scattering variation within the fault, acquired around the X point with $\sim$2 mrad collection angle. The authors presented an interpretation based on a qualitative comparison with the projected phonon DOS in the acoustic regime, where long-wavelength optical polaritons are not expected to be relevant. Additional theoretical models are still needed to identify which phonon modes in structural defects are probed by the fast electron and how they contribute to the loss signal [80]. The exploration of phonon properties of defects has just started, and a large variety of structural defects still await to be further studied at a deeper level.

Atom-size systems

Vacancies and impurities are other important structural systems that affect material properties. The presence of those entities in crystals leads to the generation of new vibration modes denominated localized, gap and resonant modes, which were intensely studied in the past with other spectroscopy techniques [82]. The first two types of modes usually appear above the phonon bands and between the optical and acoustic bands, respectively. Their displacement eigenvectors do not possess wave-like dependence in space, like bulk phonons, but are strongly peaked at the impurity position and decay rapidly within one or two atomic spacings. In contrast, resonant (quasi-normal) modes are not spatially localized and usually result in a large variety of oscillating eigenvectors that contribute to an enhanced amplitude around the impurity. Those modes couple with the external probe and result in a broad spectral resonance composed of an envelope of modes.

The vibEELS signal obtained from a single impurity/vacancy within a crystal might be hindered by bulk/surface

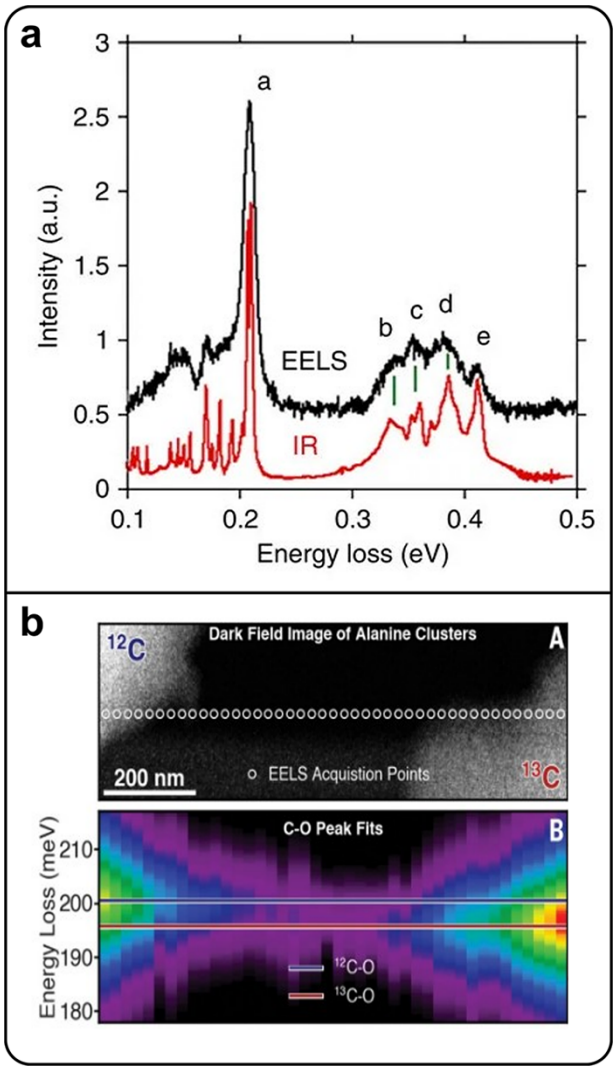

Fig. 6. vibEELS for biomaterials. (a) EEL spectra acquired 30 nm from the edge of a guanine crystal with five stretching modes highlighted, compared to a Fourier-transform IR spectrum of guanine. (Adapted from [86].) (b) Top: dark-field image of ^{12}C and ^{13}C-alanine clusters and bottom: Lorentzian fits of magnitude and position of the C–O stretch EELS peak at each point along the EELS acquisition line in the dark-field image, revealing an energy shift correlated with the locations of each isotopic alanine cluster. (From [88]. Adapted with permission from AAAS.)

phonon signal, thus atomically thin layers with adatoms represent a suitable system to study these localized excitations. Hage *et al.* [81] probed the pseudo-localized (resonant) modes of a single substitutional Si atom in a graphene layer by collecting high-angle scattered electrons using an off-axis configuration. Localization of the signal is illustrated in Fig. 5c by the EELS data acquired at different locations. EELS data interpretation was presented based on comparison with the projected phonon DOS, a quantity that includes all available phonon states of the composite system. Two modes with polarization along the graphene plane were proposed as responsible for reproducing the EELS fine structure. From the proposed oscillating geometries, it seems that one of the modes is optically inactive, only accessible with electron probes. This result illustrates the importance of spatially resolved EELS for the study of local properties with atomic sensitivity.

On the theoretical front, efforts were made to study the vibrational response of molecular-like systems [83,84], including atom-thick layers with isotopic substitution [85]. Those models predicted strong variations of the scattering signal within sub-lattice distances, which await experimental validation.

Vibrational response of beam-sensitive organic materials

Aloof spectroscopy is typically used to analyse the vibrational response of nanoscale structures in the dipole limit. The fact that the beam does not intersect the structure brings important advantages in minimizing knock-on and radiolysis damage [56]. This potential was recognized in the early stages of vibEELS and applied to study small volumes of beam-sensitive materials. Some examples include guanine flakes, proteins, L-alanine amino acids, water and metal-glass composites.

Rez *et al.* [86] selectively probed several functional groups in guanine crystals (Fig. 6a) in their native state. They identified several vibrational modes, including the C=O, C–H, N–H and mode variants of NH_2 in good agreement with far-field IR data, indicating the dipole mechanism dominance.

Furthermore, their analysis showed that in aloof mode at distances > 30 nm, the beam damage is substantially minimized. Recently, March *et al.* [87] analysed the molecular orientation of proteins (e.g. bacteriorhodopsin) with respect to the beam direction, showing that polar bonds aligned at specific orientations contribute prominently to the EELS spectrum. Other acquisition approaches, such as the scanning leapfrog, can also bring benefits under certain experimental conditions [47].

Hachtel *et al.* [88] investigated the vibrational response of amino acids with different isotopic labels. EEL spectra show a rich fine structure with a predominant peak from the C–O stretch mode (∼ 198 meV) of the carboxylate group, which shifts with different isotopic configurations. Understanding spectral shifts requires a deep understanding of how the isotopic substitution, which usually modifies the interactions between different atoms and the displacements of several nuclei, affects the whole stretching mode. To account for this complex process, realistic theories are required to properly treat the vibrational response of complex biomaterials.

Figure 6b shows a 2D map obtained from two alanine clusters separated by about 50 nm, where a spectral shift of about 4 meV can be clearly observed [88]. Interestingly, despite the proximity, dipole–dipole (associated with oscillating bonds) interaction between the alanine clusters was not reported, which represents a quite different behaviour than typical interactions between neighbouring dielectric structures.

Another interesting example is the case of water. By using a liquid cell, liquid water isotopes (H_2O and D_2O) were confined and analysed via vibEELS [89], identifying the O–H stretch mode (∼ 400 meV) and O–D stretch mode (310 meV). Ice crystals were also analysed by cooling the water specimen down to ∼ 150 K [12], and a broadband resonance associated with contributions from the O–H stretch mode was identified. Crozier *et al.* [90] also showed that a similar spectral response can be observed in nanomaterials containing hydroxides or with adsorbed water species. Moreover, Collins *et al.* [91] mapped carboxylate and imidazolate linkers in a metal-organic framework crystal-glass composite material. They were able to identify small domains (< 100 nm) with recorded spatial resolution < 15 nm at the interfaces.

Despite these advancements offering alternatives to 'damage-free' compositional analysis of functional groups and imaging of biomaterials, vibEELS for biomaterials is still in its early stages, trailing behind standard optical techniques in terms of energy resolution. For instance, SNOM has reached sub-meV energy resolution with 10 nm spatial resolution. Also, the sample preparation of a large variety of bio-specimens (e.g. viruses and proteins) in their native state, but compatible with the vacuum environment of TEMs, is a big barrier to overcome. Determining the vibrational modes of complex biological structures and developing modelling of the inelastic scattering from those modes and their interaction also remains to be achieved.

Nanoscale properties: temperature and photonic density of states

Inelastic electron scattering from phonons or vibrational modes in isolated nanostructures is linked to certain material properties, such as temperature, LEMDOS, partial phonon DOS, etc. The study and quantification of these properties rely on two important aspects: the extraction of the inelastic scattering signal from the spectrum and the adequate interpretation of the measured EELS signal. Here we focus on advances in measuring the temperature and LEMDOS in nanoscale systems.

To measure temperature, researchers have capitalized on the Principle of Detailed Balancing (PDB) which states that in a single scattering event, the energy loss and energy gain probabilities in a system at thermal equilibrium are linked by the Boltzmann factor, a quantity that depends on the system temperature. Loss and gain contributions include a Bose–Einstein population term (n) and usually appear in the EELS spectra as strong contributions at very low energies [92]. In the early 60's, both energy gain and loss processes were analysed in HR-EELS experiments using micrometre-sized electron probes scattered off surfaces [93]. More recently, using transmitted electron beams, Idrobo *et al.* [94] used surface optical modes from micrometre-size flakes, while Lagos *et al.* [55] used acoustic phonons in a single nanoparticle to measure local temperature (Figs. 7a, b). Nanostructures were heated up to high temperatures (∼ 1000 K) resulting in scattering signal driven primarily by phonon population statistics. Analysis of this spectral shift was also used later to determine the object temperature [95].

By plotting the ratio between energy gain and loss scattering as a function of excitation energy, a curve with linear behaviour can be obtained (Fig. 7c) and the temperature can be determined with high precision (down to 1 K) from the slope fit [55]. Limitations on the instrumental energy resolution (> 15 meV) affect the measurement accuracy and produce deviations from this linearity [55]. This linear behaviour also shows that PDB holds for a single phonon scattering event.

The spatial resolution of the temperature measurement is related to the delocalization degree of the vibEELS signal used in the thermal analysis. Dipole signal might provide resolution on the order of the nanostructure size due to the excitation of delocalized modes [49,97], while impact scattering signal can provide sub-lattice sensitivity (Fig. 5a).

An important property of a photonic structure is the LEMDOS, which shows how the electromagnetic energy and fields are localized in space. In 2008, García de Abajo and Kociak [98] proposed a relationship between the scattering probability of a localized surface plasmon and the corresponding LEMDOS. The relationship is valid for isotropic dielectric particles in the dipole limit and was deeply investigated in numerous physical systems [99]. More recently, Lourenço-Martins *et al.* [49] extended the relationship to optical surface phonons using the same arguments.

Li *et al.* [96] conducted tomography studies to fully reconstruct the phononic LEMDOS in a MgO nanocube (Fig. 7d). Their results illustrate the localization of the three surface optical modes (e.g. Fig. 4a), confirming their spatial distribution and revealing richer spatial information regarding the face modes, which show strong localization towards the cube edges. Furthermore, their full reconstruction results show an asymmetric effect in the distribution of the corner modes due to the interaction with the substrate. As mentioned earlier, the substrate can alter the landscape of available surface phonon modes in the composite particle–substrate system and its presence and influence on the local environment must be considered when assessing local thermal and LEMDOS properties at the nanoscale.

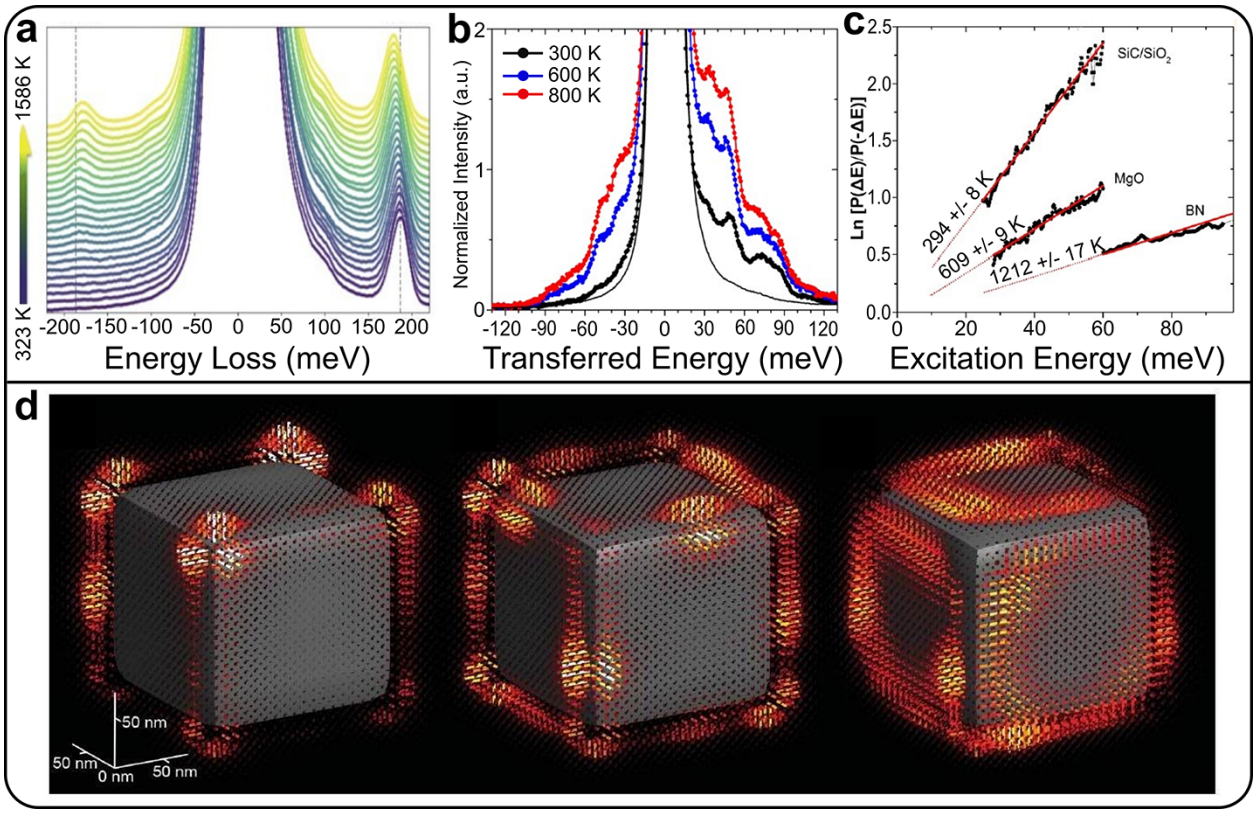

Fig. 7. Measurement of nanoscale properties via vibEELS. (a) EELS and Electron Energy Gain Spectroscopy (EEGS) peaks of an optical surface phonon mode in *h*-BN as a function of temperature. (Adapted figure with permission from [94], © 2018 by the American Physical Society.) (b) EELS and EEGS peaks of bulk phonon excitations in an MgO nanocube at three different temperatures, and (c) high-precision temperature derivation from a linear fit of the logarithm of the loss over gain ratio as a function of energy for different materials. (Adapted with permission from [55]. Copyright 2018 American Chemical Society.) (d) 3D reconstruction of the LEMDOS of three components of the SPhP response of an MgO cube. (From [96]. Adapted with permission from AAAS.)

Spectroscopy of plasmons

In addition to the numerous applications and new physics unveiled using vibEELS, performing low-loss EELS on metallic or metal-like materials reveals the collective behaviour of charge carriers in these materials. The first description of collective oscillations of electrons in a solid was presented in the 1950s by Pines and Bohm [100–102], who used a collective description of motion to describe long-range interactions and organized 'plasma oscillations' in a free electron gas. They describe the response to a fast charged particle moving through the electron gas and setting up long-range oscillations via Coulomb interactions. In 1957, Ritchie [103] extended this theory, using a hydrodynamic model, to predict the collective oscillations and coining the word 'plasmon' to describe a plasma oscillation. Ritchie considered the metal dielectric as a function of both frequency and wavevector and with appropriate boundary conditions was able to derive the surface plasmon frequency and predict the quantized energy loss of a fast electron moving through a thin metal film. This phenomenon was soon observed experimentally by Powell and Swan [104]. Initial studies on plasmonic particles measured the energy lost by a passing fast electron using EELS and were carried out using broad beam illumination over a wide area, giving the average plasmonic response with limited spatial information (e.g. [104–106]) but, even in these early studies, providing information on the dispersion behaviour of the surface plasmons [62,107].

The use of energy-filtered imaging opened up the possibilities for nm-resolution spatial mapping of plasmonic modes in the electron microscope [108–112]. However, the energy resolution of these systems limited the accessible energy ranges to the visible–ultraviolet (UV) range of the electromagnetic spectrum. Further advances applied STEM spectrum-imaging [113] and monochromator technology to allow researchers to push the spectral range into the NIR and MIR [114,115].

The importance of studying IR–visible (IR-vis) plasmonics is mainly due to the crucial applications of these materials in different areas such as nanophotonic circuitry [116–118], surface-enhanced infrared absorption, surface-enhanced Raman spectroscopy [119–125] and plasmon-enhanced photochemistry [126–130]. The application of EELS techniques for characterizing nanoparticle systems is thoroughly reviewed by Wu *et al.* [131] and in an invaluable review by García de Abajo [132]. The following sections review recent progress in EELS studies of IR plasmonics in metallic systems and in new plasmonic materials.

Infrared surface plasmonics in metallic structures

Noble metals may be considered lossy for plasmonic applications due to their high energy interband transitions, but at lower energies they usually exhibit Drude-type behaviour. Therefore, materials such as silver (Ag), gold (Au) and copper (Cu) typically perform well in the NIR-vis spectral regime.

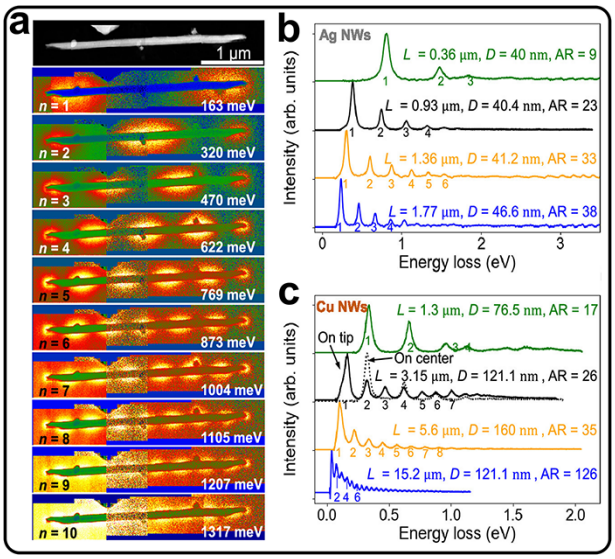

Fig. 8. Plasmonic response of a Cu NW. (a) High angle annular dark field micrograph from a 3.15 μm Cu NW and corresponding EELS maps of different SPR modes at the energies indicated. EELS spectra obtained from (b) Ag NWs and (c) Cu NWs of different lengths and aspect ratios. (Adapted with permission from [143]. © 2021 American Chemical Society.)

However, since the majority of plasmonic metals, such as aluminium (Al), have plasma frequencies in the vis-UV range and above, strategies such as alloying or controlling the size and shape of the system are necessary for designing IR-active systems [133–136]. In the upcoming sections, we review recent studies on plasmon activity in the NIR-vis range in different 1D, 2D and 3D geometries.

1D designs

In metallic systems, NWs are one of the most well-studied geometries for supporting IR surface plasmons. In NW systems, the simple expediency of increasing the length provides the medium for low-energy surface plasmons to resonate, with the resonant energy dependent on the length, aspect ratio and material used. Among different metals, Ag is one of the most common media for plasmonic applications at NIR-vis wavelengths [28,114,131,137]. This popularity is because of the low damping properties of Ag in this spectral regime, since it is a highly conductive metal with an interband transition around 3.8 eV, in the near-UV [138,139]. LSPRs, Fabry–Perot (FP) type SPP resonance behaviour and the impact of geometrical defects on the SPRs in Ag NWs have been thoroughly probed using spatially resolved STEM-EELS [28,114,140]. These early results show the power of EELS for resolving LSPR nodal distributions in energy and space, paving the road for more detailed studies in this area [141].

Other metals, including gold, copper and aluminium, are also extensively used for a wide variety of IR surface plasmon applications, although they are considered more lossy than silver due to their lower-energy interband transitions. However, with respect to Au NW systems, a recently published study by Wu *et al.* on FP resonances using STEM-EELS revealed that some of the resonance modes in Au NWs of different lengths (from 0.5 μm to 10 μm) have dephasing times twice those predicted [142]. Similarly, Mkhitaryan *et al.* demonstrated that IR and visible surface plasmon resonances in long Cu NWs (1.3 μm to 15.2 μm) have a high quality factor, comparable with IR responses in long Ag NWs (0.3 μm to 1.8 μm), again exceeding expectations from previous studies [143] (Fig. 8). According to their calculations of the Cu NW cross-section, a considerable amount of electromagnetic energy generated by SPs in Cu NWs resides outside of the metal, implying that internal Ohmic resistance in the Cu NW will not greatly affect the SPP propagation. In a study on Al antennas (around 2.4 μm to 4 μm long NWs), Lagos *et al.* demonstrate their performance at energies down to the MIR in coupled plasmon–phonon platforms, exhibiting a quality factor comparable with that achievable in gold antennas [144]. These findings open new doors for further investigations on other metals which are typically considered lossy for IR-vis plasmonic applications.

2D and 3D designs

Other common strategies for manipulating IR plasmonic properties to produce other optical properties in metallic nanostructures, such as a broadband spectral response, include increasing the dimensionality of the structure and introducing geometrical complexities. Usually, an increase in size or structural complexity in plasmonic systems leads towards spectral complexity, and the system may show multiband or broadband plasmonic properties rooted in corner, edge, or cavity plasmon modes and in mode hybridization and coupling [145–150]. In this regard, EELS has heavily contributed to understanding the impact of size and shape variations on the spectral and modal distribution of plasmons in different structures. As an example, Campos *et al.* demonstrated the non-equivalent dispersion of edge modes and cavity modes, visualizing 2D standing waves of optically dark cavity modes in Al nanotriangles [151], while Bellido *et al.* identified characteristic edge units and fractal scaling laws in Ag Koch nanofractals, concluding that as structural complexity increases, spectral complexity does too [152].

The resolving power of EELS in revealing even minor changes in surface plasmon spectral footprint has made this technique an excellent candidate for probing naturally formed or intentionally shaped defects, imperfections and anomalies

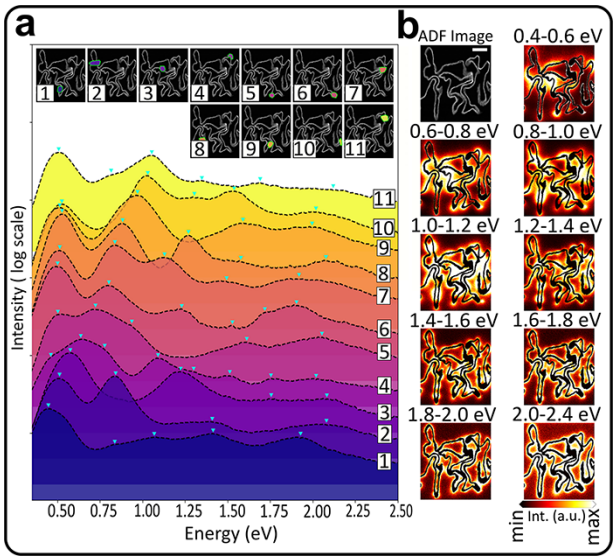

Fig. 9. Plasmonic response of a complex randomized wrinkled gold film. (a) EELS spectra from different locations of a wrinkled gold nanostructure demonstrating the broadband LSPR of the system. (b) Energy-resolved EELS maps show the evolution of surface plasmon hotspots with energy. The scale bar is 200 nm. (Adapted from [146], with the permission of AIP Publishing.)

[152–157]. Using STEM-EELS combined with high spatial resolution tomography, de Oliveira *et al.* were able to detect LSPR peak broadening caused by a single atomic-sized defect (dislocation) at the junction of two gold nanorods welded using a femtosecond laser [153].

Although in de Oliveira's work, LSPR peak broadening was used as a meter to judge the quality of the weld, structural defects can be designed into the geometry as a means to tune the surface plasmon response for different applications. In this regard, introducing nanoscale defects, such as cavities and gaps, can be considered as a strategy to adjust the surface plasmon resonance energy. EELS studies done by Genç *et al.* on AgAu nano-boxes, pinholed nano-boxes and nanoframes demonstrate the tunability of plasmon responses from UV wavelengths to IR, for biomedical purposes [156]. EELS results shown in this work suggest the possible hybridization of the inner and outer surface plasmon modes of the nanoframe, resulting in intense homogeneous responses from these structures [156]. The impact of having nanometre-sized apertures at the centre of 2D triangular Sierpiński nanostructures can also be found in research by Bicket *et al.* [155]. According to their work, introducing these apertures causes redshifting of the plasmon peaks, allowing the structure to couple to longer wavelengths without increasing its spatial footprint [155]. Further experiments using both spatially resolved and momentum-resolved STEM-EELS have revealed that the introduction of a point defect into a plasmonic crystal alters the photonic bandstructure, creating a defect state in the crystal's bandgap [158].

Another important geometrical feature that can locally affect plasmon activity is a nanogap. Nanogaps can support strongly confined surface plasmon hotspots that STEM-EELS is usually able to detect [159]. By combining STEM-EELS and different simulation techniques, other physical phenomena around gaps such as plasmon mode hybridization [145,160], coupling [161] and plasmonic Fano resonances and anti-resonances at IR energies have been thoroughly investigated [162] and recently reviewed [163].

The findings regarding the relationship between the structural and spectral complexity have greatly assisted researchers in designing systems with desired plasmonic responses. Bicket *et al.*'s study on the plasmonic properties of iterative Sierpiński fractals is an example of using LSPR hybridization to build multiband surface plasmon antennas [150]. The idea of using surface plasmon hybridization for controlling plasmonic response is nevertheless not limited to controlled 2D designs. Recently, researchers have benefited from structural feature randomization to create structures with broadband surface plasmon responses from MIR to near-UV energies. For example, Wang *et al.* used randomly formed silver fractal dendrites to achieve a broadband SP response. According to the EELS results, the electromagnetic hotspots of dendritic nanostructures are highly localized (domains with sizes below 0.4 μm) and are promoted by the randomness of geometrical features and the multi-scale features of the fractal [148].

In Mousavi *et al.*'s study on continuous wrinkled gold films, the combination of random structural features and extremely large system sizes (on the order of millimetres) leads to surface plasmon activity from the MIR to visible regime. As is highlighted by their spectroscopy results, the wide energy range of the SP response is extremely affected by the large continuous shape of the structures, plasmon coupling and hybridization around sharp bends in the structure, and differently sized nanogaps (down to a few nm) [146,147] (Fig. 9).

Similar to the SPhP example discussed above, EELS scattering in plasmonic samples gives insight into the LEMDOS [98]. Recent advancements in STEM-EELS tomography have made it possible to study surface plasmons in three dimensions [164–168]. As an example, Haberfehlner *et al.* conducted a comprehensive investigation on the 3D surface plasmon response of vertically coupled nanoparticle dimers, as shown in Fig. 10 [168], studying bonding and anti-bonding modes in coupled nanotriangles of different sizes (140, 190, 240 and 340 nm) (Figs. 10c, d). The application of STEM-EELS tomography to probe the 3D LEMDOS of plasmonic systems

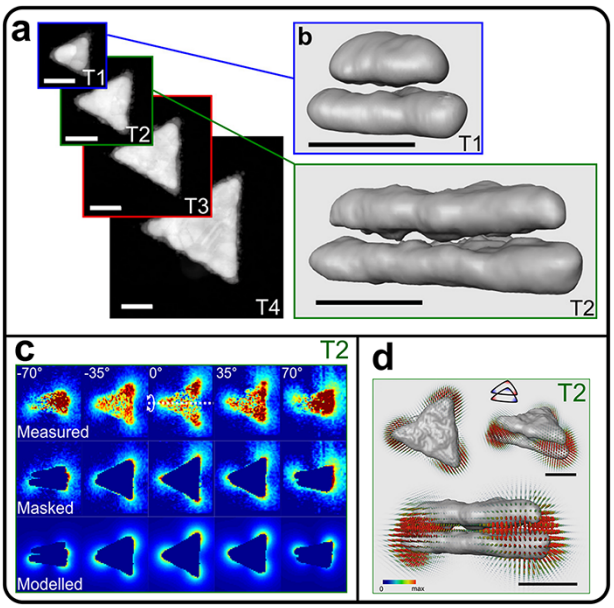

Fig. 10. Tomographic reconstructions of the plasmonic response of a triangular nanoprism dimer. (a) High-angle annular dark-field micrographs of fabricated triangular nanoprism dimers with different sizes (scalebars are 100 nm) and (b) tomographic reconstructions of T1 and T2. (c) EELS maps of the T2 dimer, acquired at different tilt angles as indicated, for a low-energy bonding mode (1.02 eV), representing the experimental energy-resolved maps (top row), maps with the particles masked (middle) and reprojected (modelled) maps (bottom). (d) Tomographic reconstruction of the photonic local density of states of the low-energy bonding mode in T2. (Adapted from [168].)

is also demonstrated in works by Nicoletti *et al.* [164], Collins *et al.* [165,166] and Hörl *et al.* [167].

New materials

Noble metals have provided consistent choices for plasmonic applications, but their use in the IR suffers from several drawbacks that entice researchers to turn to alternative materials with more freedom in tuning the plasma frequency over the spectral range of interest [169–173]. Noble metals typically support a plasma frequency (ω_p) in the vis-UV range of the spectrum, while in the MIR-NIR, the plasmonic response is far from ω_p. In the visible region, several of the more popular metals suffer from interband transitions, while deep in the IR, these metals have high imaginary components of their dielectric function and the plasmon response suffers from intraband damping, limiting plasmon lifetime and propagation length. Using a material with ω_p closer to the spectral region of interest results in lower damping contributions from intraband transitions and thereby longer plasmon lifetimes. In addition, further down the polariton dispersion curve, away from ω_p, the confinement factor of the SP is reduced, to the extent that the evanescent fields may extend several free-space wavelengths into the dielectric medium [174]. At this point, the advantage of sub-diffraction confinement of EM energy in such a material is lost, bringing forward interest in spoof SPPs [175,176], which have not yet been studied with EELS. This phenomenon limits the application of noble metals in the longer wavelength range of the IR, especially when sub-wavelength field confinement is required. Another constraint on many potential applications is the compatibility with semiconductor manufacturing processes.

All of these factors inspire research interest in alternative plasmonic materials such as heavily doped semiconductors, which may have charge carrier densities on the order of 10^{18}–10^{21}cm^{-3}, lower than the conduction electron density in classical plasmonic metals (typically on the order of 10^{22}cm^{-3}). As a result, doped semiconductors tend to support bulk plasmons in the IR region of the spectrum ($\omega_p < 1.5$ eV). Alternative materials for semiconductor-based plasmonics include vacancy-doped materials such as copper chalcogenides, or impurity-doped semiconductors or metal oxides, such as the tungsten bronzes, indium tin oxide or zinc oxide [177,178]. Metal oxides, particularly transparent conducting oxides, are particularly desirable for their applications in new optoelectronic technology.

Vacancy-doped copper chalcogenides

Copper vacancies act as *p*-dopants in copper chalcogenide materials, contributing to high charge carrier densities and allowing these materials to support LSPR resonances dependent on the precise structural and stoichiometric properties [177,178]. EELS studies of copper selenide [182], copper telluride [183] and copper phosphide [179] allow direct quantification of the vacancy concentration correlated with surface plasmon activity in a single nanoparticle. For example, Bertoni *et al.* [179] used contrast changes in high spatial resolution STEM imaging to quantify the vacancy concentration in a single $Cu_{3-x}P$ nanocrystal (Figure 11a), observing two LSPR modes in the same nanocrystal. Willhammar *et al.* [183] used high resolution-STEM tomography to identify long-range order in Cu vacancies in CuTe, revealing vacancy channels in a plasmonically active nanoparticle and confirming through density functional theory and EELS simulations that surface plasmon activity appears only in vacancy-rich CuTe. In another approach, Casu *et al.* [182] used core-loss EELS to quantify the stoichiometry of $Cu_{2-x}Se$ nanocrystals during *in situ* annealing, observing a partial loss of Cu (from 2.01:1 to 1.91:1 Cu:Se ratio) upon heating and correlating

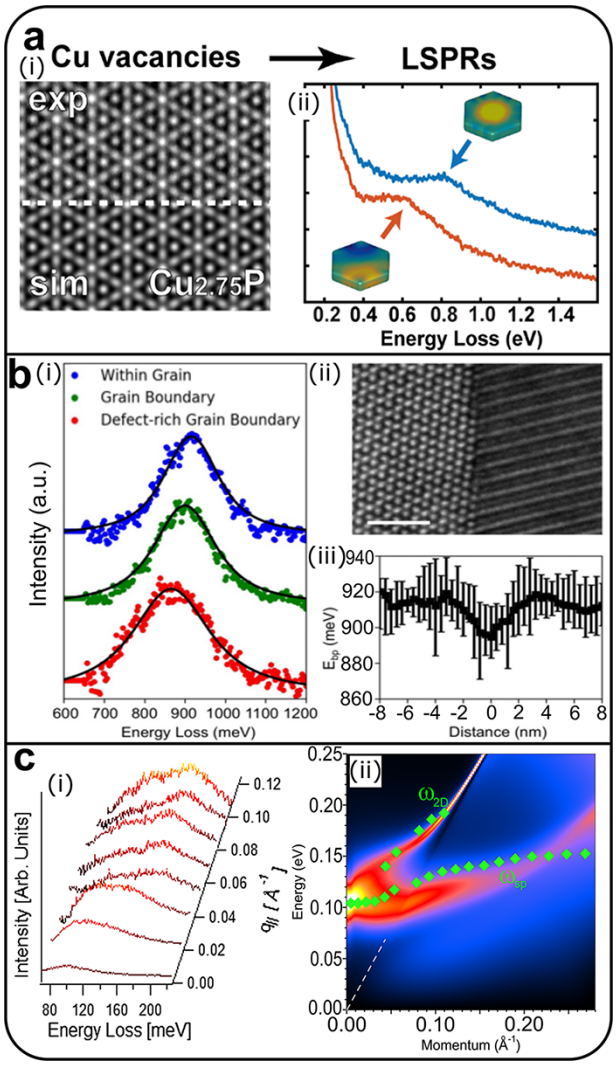

Fig. 11. Plasmonically active semiconductor materials. (a) (i) Experimental and simulated high-resolution ADF-STEM image of a $Cu_{2.75}P$ nanocrystal and (ii) low-loss EELS spectra of two plasmon peaks in the vacancy-doped nanocrystal. (Adapted with permission from [179]. Copyright 2019 American Chemical Society.) (b) (i) Bulk carrier plasmon peaks near grain boundaries; (ii) High resolution ADF-STEM image of the grain boundary for the green spectrum in (i); and (iii) energy of the bulk plasmon peak as a function of distance from the grain boundary in (ii). (Adapted with permission from [180], © 2020 by the American Physical Society.) (c) (i) Momentum-resolved HR-EELS spectra for a Bi_2Se_3 topological insulator film, exhibiting two distinct plasmon peaks; (ii) surface loss function calculated for a two-component system with carrier plasmons and Dirac plasmons, green diamonds indicate fitted peak positions of experimental data. (Adapted with permission from [181]. © 2015 by the American Physical Society.)

this loss with the appearance of a spectral feature attributed to LSPR (1.1 eV).

Tungsten bronze

Tungsten bronzes are WO_3-based materials which form a solid solution with metal ions (M_xWO_3), typically alkali metals; these materials possess bulk plasmons in the visible or NIR regions of the spectrum. No plasmonic response is observed in non-metallic WO_3 particles, but plasmonic activity can be detected with even a small addition of Na [184], becoming stronger and blueshifting with increasing Na concentration [185], until its plasmonic response rivals that of gold [184]. EELS studies have identified corner and edge LSPR modes and bulk plasmon peaks in Na_xWO_3 nanocubes and nanocrystals, from $x = 0.66$ [184] to $x = 0.83$ [185].

Another tungsten bronze, Cs_xWO_3, is used in heat-shielding applications and possesses two peaks in the NIR-vis region of the spectrum. Initial work by Sato *et al.* [186] attributed these peaks to two bulk plasmons: one from carrier electrons contributed by Cs dopants and the higher energy peak from excitation of valence electrons; they also identify a Cs deficiency near the surface of their $Cs_{0.33}WO_3$ particles, transforming the surface into an insulating material and redshifting the observed surface plasmon energy, thereby highlighting one possible effect that non-uniform doping may have on plasmonic activity in semiconducting materials. Further work by Sato *et al.* [187] using momentum-resolved EELS reveals that the low energy and high energy peaks are present along different axes of the hexagonal crystal structure. They demonstrate that the anistropy of the crystal structure is reflected in the anisotropic electronic band structure and plasmonic response, wherein the low-energy peak corresponds to a highly damped plasmon along the *ab*-axis, while the higher energy peak corresponds to a plasmon along the *c*-axis with lower damping. The anisotropic response of these

nanoparticles was further probed by Machida *et al.* [188], who used the relative orientation of different nanoparticles to the electron beam to observe lower-energy peaks perpendicular to the *c*-axis and higher-energy peaks parallel to the *c*-axis.

Doped indium oxide

Indium oxide doped with tin (i.e. indium tin oxide, ITO) and, optionally, with fluorine has been one of the more popular materials for studying semiconductor NIR plasmonics. ITO has no interband transition in the IR-visible regime of the spectrum and, when highly n-doped, has a high bandgap and exhibits optical transparency, a feature which is desirable for many applications. In EELS, studies have been done on ITO films [180], lithographed prisms [189] and wet-chemistry-grown nanocubes or semi-spherical particles [190–193], taking advantage of the explicit presence of the bulk plasmon peak in the EELS spectrum to characterize the effect of doping. The plasmonic response of ITO is fuelled by conduction electrons contributed by either tin dopants or the presence of oxygen vacancies in the lattice, with the level of tin doping providing the dominant method of control over the plasmonic response.

Increasing the level of tin doping can increase the carrier density to concentrations on the order of 10^{21}cm^{-3}, reducing the resistivity of the material and blueshifting the surface and bulk plasmon peaks. In one study by Olafsson *et al.* [194], the bulk plasmon EELS peak shifts from 705 meV for 1 at% Sn to 1575 meV for 10 at% Sn. Increasing the Sn concentration beyond 10 at% then causes the bulk plasmon to redshift again, likely due to an increase in ionized impurity scattering from the additional dopant concentration [190]. Yazdi *et al.* [195] also observed a change in the decay length of the LSPR evanescent fields correlated with dopant distribution in core and shell co-doped F/Sn indium oxide. EELS studies have also demonstrated that arrays and nanoclusters of ITO nanocubes support highly localized IR-frequency electric fields in extremely small cavities between the cubes [190,192]. Addition of fluorine dopants to ITO is less well studied but provides morphology control of nanoparticles grown in solution through surface passivation [190,191] and enhances the quality factor of the LSPR [190] by filling in oxygen vacancies, thereby reducing oxygen vacancy scattering [190,192].

At a constant doping concentration, Kapetanovic *et al.* [189] mapped LSPR and bulk plasmon modes in lithographed ITO triangular nanoprisms before and after rapid thermal annealing, demonstrating that the annealing process improves the quality factor of the LSPR peaks and increases the bulk plasmon energy by over 100 meV, attributed to a reduction in resistivity and an increase in carrier density. In thin ITO films, Yang *et al.* [180] use spatially resolved EELS to reveal a redshift in the bulk plasmon near grain boundaries (Fig. 11b), due to the structural disorder and disruption of electronic properties caused by the grain boundary. This research begins to reveal the sensitivity of the plasmonic response to structural defects and charge carrier generation mechanisms in highly doped materials.

ZnO

Another transparent conducting oxide of interest for NIR plasmonics is ZnO, doped with either Ga or Al to increase the carrier density while minimizing lattice distortions. ZnO has a high bandgap and exciton binding energy, leaving the NIR region of the spectrum free of interband transitions and open for plasmonic activity. So far, doped ZnO has not been studied intensely in EELS, but a study by Granerød *et al.* [196] on heavily Ga-doped ZnO (GZO) uses the high resolution of STEM imaging to correlate local Burstein–Moss bandgap shifts with plasmon resonance wavelength. They analyse the local relationship between bandgap energy and plasmon energy in a ZnO/GZO thin film heterostructure, identifying a conduction band bulk plasmon and a surface plasmon at 0.56 eV supported by the GZO, with no observable surface plasmon on the undoped ZnO film [196].

Topological insulators

Topological insulators (TIs) present very interesting plasmonic responses because of their unique surface properties. Plasmonic behaviour in TIs such as bismuth- or antimony-based binary and ternary chalcogenides has been detected in the IR [197,198] and in the UV [199–202]. Bi_2Se_3, for example, supports both a Dirac plasmon in the 2D electron gas on the surface and a carrier plasmon from conducting charge carriers in the material [181,197,198]. These two plasmon responses overlap in energy as $\mathbf{q} \rightarrow 0$ but can be distinguished by their different dispersion curves, as observed in momentum-resolved HR-EELS (Fig. 11c) [181].

Towards higher energy, STEM-EELS reveals that pinhole defects in Bi_2Te_3-Sb_2Te_3 heterostructure nanoplates locally enhance the UV-vis LSPR and that local compositional changes shift the LSPR energy [199,200]. Cha *et al.* [201] have also used EELS to retrieve the optical response of binary and ternary chalcogenides as a function of 2D layer thickness, composition and intercalation of small organic molecules in between chalcogenide layers. They demonstrate blueshifting of the surface plasmon energy by several eV in Bi_2Se_3 with increasing layer thickness and a linear dependence of the plasmon peak energy on Se fraction in the ternary chalcogenide $Bi_2(Se_xTe_{1-x})$, attributing the observed blueshift to a change in the lattice constant as Te is replaced by Se. Intercalation of small molecules or metal ions also changes the optical response; intercalated organic molecules enhance a low-energy photonic guided mode peak, possibly due to changes to the stack's dielectric function, while the introduction of Cu ions suppresses both the photonic mode and the plasmon response.

Semiconductor and metallic systems for high-energy plasmonics

Other new plasmonic materials show activity in the UV range of the spectrum, detectable with microscopes of lower energy resolution. EELS remains useful for studying these materials because it can reveal the response over a wide spectral range that can be difficult to access with photonic probes and detectors, from the visible to the extreme UV (EUV).

For example, although the alkali and alkaline earth metals are known to have high conduction electron densities suitable for UV plasmonics, their high reactivity makes them difficult to probe experimentally. This difficulty has been overcome in preliminary work by Yang and Crozier [203], who use the electron beam to reduce NaCl to Na-metal under vacuum and subsequently detect the Na bulk plasmon at 6 eV, with lower energy peaks attributed to surface plasmon excitation

in small sodium particles. Biggins *et al.* [204] study Mg hexagonal nanoplates protected by a few-nm MgO layer, observing a strong bulk plasmon around 10 eV and a series of LSPR modes down to 1.9 eV corresponding to a set of corner, edge and cavity modes relevant to the hexagonal symmetry.

At even higher energy, Shekhar *et al.* [205] studied undoped silicon, which behaves like a free-electron metal in the EUV, supporting a valence band bulk plasmon at 16 eV and SPP behaviour between 5 and 11.5 eV. They use momentum-resolved TEM-EELS to map the dispersion relation of the Si SPP and also of lower-energy Cherenkov radiation. Manfrinato *et al.* [206] have also shown that the volume plasmon of Si can be blueshifted by up to 1.2 eV from the bulk value by reducing the size of lithographed Si nanostructures down to 1.1 nm. They identify, in a wedge-shaped Si nanostructure, shifts of the bulk plasmon energy as a function of location along the wedge, and LSPR down to approximately 4 eV. They suggest that a combination of boundary effects and changes to the electronic band structure due to quantum confinement may be the cause of the observed bulk plasmon energy blueshifts.

Likewise, both Borja-Urby *et al.* [207] and Wang *et al.* [208] found blueshifts of the bulk plasmon in elemental bismuth nanoparticles. Wang *et al.* observe that the bulk plasmon EELS peak broadens and blueshifts from ~ 14 eV, up to >28 eV for 5-nm particles, beginning noticeable blueshifting when the particle size is decreased below 40 nm. They attribute this shift to the effect of a semi-metal to semiconductor transition due to quantum confinement effects, previously observed in other bismuth nanoparticles, in addition to the effects that limiting particle size have in limiting the available bulk plasmon wavevectors. Limiting the particle size cuts the available **q**-vectors, modifying the bulk plasmon dispersion curve and thereby affecting the observed bulk plasmon energy. Aside from the behaviour of the bulk plasmon, further EELS studies on bismuth quantum dots (QDs) on a magnetic yttrium iron garnet (YIG) substrate reveal enhancement of LSPR signal near the Bi–YIG interface, with further potential for exploring interesting spin-orbit field interactions with Bi LSPR modes [209].

Spectroscopy of strongly coupled modes

In addition to the many interesting applications for pure plasmonic or vibrational modes, the prospect of coupling two excitations together opens up additional possibilities to control the optical response of a system beyond the standard tuning approaches remarked upon above. Coupling occurs when two excitations interact strongly enough to modify the properties of one or both. If the coupling is strong enough, a new system is formed with normal modes possessing hybrid characteristics from both components. Strong coupling conditions are met when the coupling constant is larger than the combined decay rate of the system components: instead of decaying and losing energy to the environment, the excitations instead exchange energy (Rabi oscillations), sustaining the hybrid mode for longer than otherwise possible for two isolated oscillators.

This behaviour is observed as an anti-crossing of energy levels in the spectral response, characterized by the Rabi splitting (energy splitting at the avoided crossing) and the detuning parameter (frequency difference between the energy levels of the two excitations in isolation) [210]. Although strong coupling phenomena have been studied in the photonic community for several decades [210,211], only recently have EELS studies begun to emerge on plasmon–exciton coupling in the NIR–visible regime and on plasmon–phonon coupling in the MIR–NIR regime, thanks to recent improvements in energy resolution.

Plasmon–exciton coupling

Some indications of coupling between a surface plasmon mode and an exciton have been observed in microscopes with limited energy resolution. Gold nanoparticles on ZnO are of interest for their applications in photocatalysis, and although plasmon–exciton coupling is not the main purpose of their studies, both Bueno-Alejo *et al.* [212] and Bertoni *et al.* [213] observed unexpected behaviour in the EELS response that they attribute to coupling between the Au LSPR and the ZnO bandgap-edge exciton. Bueno-Alejo *et al.* [212] observed small energy shifts in the LSPR peaks near the ZnO exciton energy, while although Bertoni *et al.* [213] did not observe a strong energy shift, they detected changes to the spatial localization of the ZnO exciton signal inside a gold nanoparticle on a ZnO structure. In another system, Shu *et al.* [214] use momentum-resolved TEM-EELS to observe a 2.3-eV mode with dispersion characteristics not matching those of either a plasmon or exciton, which they attribute to a hybrid mode formed from a coupled state between a π-plasmon and an exciton, both supported within 1T-$TiSe_2$.

More detailed studies on strong plasmon–exciton coupling have been performed by modifying the detuning parameter through manipulating either the LSPR energy or the exciton energy. An early study by Wei *et al.* in 2015 [215] used different sizes of silver nanoparticles to reduce the detuning between the dipolar LSPR and the bandgap-edge exciton in ZnO NWs (~ 3.4 eV). They observed anti-crossing behaviour with a Rabi splitting of up to 170 meV for well-tuned LSPRs (Fig. 12a), also observing spatial differences in the relative excitation probability of the upper and lower hybrid modes. They propose a hybridization model with symmetric and antisymmetric coupled charge distributions between the LSPR and exciton (inset in Fig. 12a(i)).

Using a similar tuning strategy, Yankovich *et al.* [216] used size to control the detuning of the dipolar LSPR of truncated silver nanopyramids relative to the exciton energy (2.03 eV) of the transition metal dichalcogenide WS_2 (Fig. 12b). Their study reveals that the relative excitation probabilities of the lower and upper hybridized peaks can be manipulated with the LSPR: exciton energy detuning parameter. They also observed that the magnitude of peak splitting in the coupled system depends on the number of WS_2 layers, with no detectable splitting using a single monolayer but up to 130 meV of Rabi splitting for a 6-layer WS_2 flake.

Conversely, Bitton *et al.* [217] manipulated QD size to study the coupling of QD excitons with both bright and dark dipolar LSPR modes of lithographed silver bowties (Fig. 12c). They demonstrated that strong coupling can occur for both bright and dark plasmonic modes with excitons of the appropriate energy, obtaining peak splitting of ~150–200 meV and ~100–160 meV, respectively. In addition, they determined that the coupling and peak splitting is strongest when the QDs are located in regions of high electric field for the specific LSPR

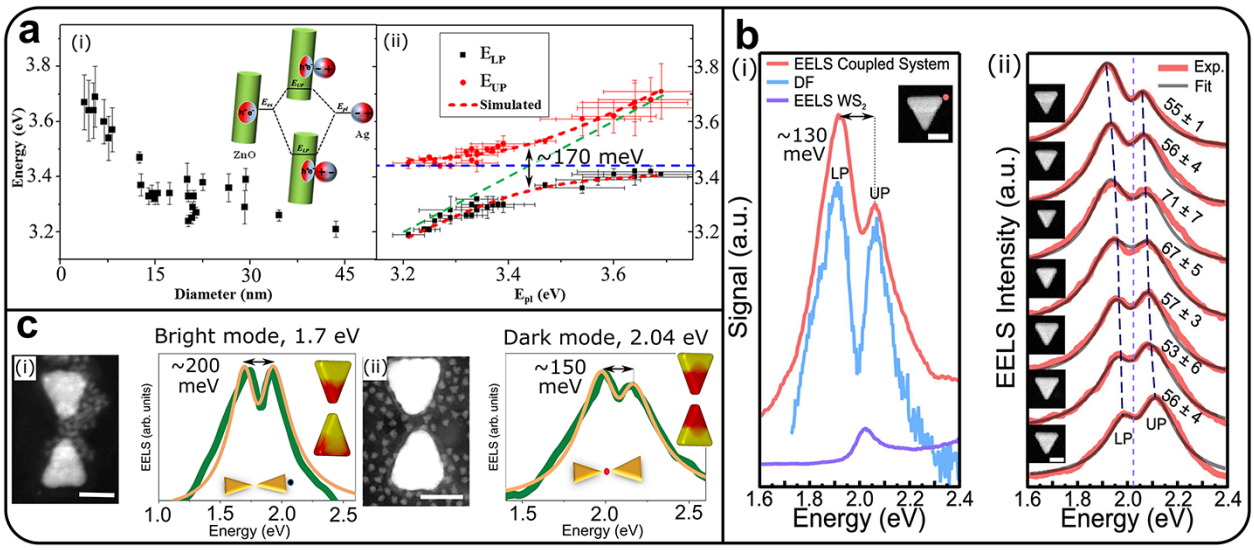

Fig. 12. Strong coupling in plasmon–exciton systems. (a) (i) The energy of a dipolar LSPR in isolated silver nanoparticles as a function of particle diameter (inset: hybridization model for coupling between the dipolar LSPR and the ZnO exciton) and (ii) the energies of two peaks obtained from plasmon–exciton coupling, as a function of isolated nanoparticle plasmon energy (green line: expected nanoparticle plasmon dispersion), showing avoided crossing behaviour near the exciton energy (blue line). (Adapted with permission from [215]. © 2015 American Chemical Society.) (b) (i) Experimental spectra (dark-field scattering and EELS) of a silver nanoprism on a 6-layer WS_2 flake and (ii) EELS spectra from triangular nanoprisms with different sizes and thereby different detuning from the WS_2 exciton energy, from a redshifted plasmon peak (top) to near-zero detuning (centre), to a blueshifted plasmon peak (bottom spectra). (Adapted with permission from [216]. © 2019 American Chemical Society.) (c) (i, iii) ADF-STEM image of silver bowties surrounded by quantum dots with an exciton energy of (i) 1.8 eV and (ii) 2.0 eV, respectively, revealing Rabi splitting observed on the bright (i) and dark (ii) dipolar LSPR modes of the bowtie. (Adapted from [217].)

mode, even though these areas may not necessarily show the strongest EELS signal.

Theoretical studies confirm the experimental results that electronic excitations can exhibit strong coupling with both bright and dark LSPR modes [218,219]. Zouros *et al.* [218] calculate Rabi splitting in a core-shell geometry, in which an excitonic material core couples with several multipolar LSPR of an Ag shell, also revealing that the Rabi splitting should be evident in far-field cathodoluminescence (CL) spectra as well, something which has not yet been confirmed experimentally. Crai *et al.* [219] pursued the near-field vs far-field question further, calculating the near-field (EELS) and far-field (CL) spectra of NW/particle-on-mirror geometries with a quantum emitter embedded between the particle and the mirror, likewise predicting Rabi splitting in both EELS and CL. Interestingly, they also conclude that in the NW-on-mirror system, which supports degenerate bright and dark LSPR modes, the Rabi oscillation dynamics are dependent on the excitation dynamics, because of different relationships between electron beam velocity and excitation probability for the bright and dark modes.

Plasmon–phonon coupling

Experimentally studying coupling behaviour between plasmons and phonons requires higher energy resolution than plasmon–exciton coupling studies, in order to probe lower energy modes in the MIR–NIR regime. Pioneering work by Tizei *et al.* in 2020 [220] demonstrates strong coupling between the plasmonic modes in a silver NW and FK vibrational modes in *h*-BN at approximately 180 meV. They use the electron beam to cut a single Ag NW progressively shorter in order to change the detuning of the dipolar LSPR mode and demonstrate anti-crossing behaviour (Fig. 13a), effectively scanning the dipolar LSPR from lower energies through to higher energies than the *h*-BN SPhP modes. They observe a Rabi splitting of up to 52 meV, finding also that the coupling strength depends on the amount of *h*-BN contained in the mode volume of the NW dipolar mode.

Capitalizing on stacked geometries and using more naturally abundant materials, Lagos *et al.* [144] demonstrate strong coupling behaviour between Al and SiO_2 NWs (Fig. 13b). They control the detuning parameter by fabricating stacked NWs of different lengths; the SiO_2 resonance is confined within the RB, while the dipolar LSPR mode of the Al NW changes significantly with length. Because of this, they are able to show the coupling behaviour through a large detuning length, observing a Rabi splitting of approximately 26 meV between peaks in the range 120–180 meV and highlighting that strong coupling conditions can be achieved by intelligent design of the coupling geometry. In addition, the authors spatially map the EELS probability of the strongly coupled hybrid modes, observing different EELS distributions for symmetrically and anti-symmetrically coupled charges across the two NWs (Fig. 13b(iii)).

On the theoretical side, calculations push the field of strong coupling as observed in EELS into the study of plasmon–vibrational mode coupling, an area which has yet to be experimentally explored. Konečńa *et al.* [141] predicted coupling between the LSPR modes of a plasmonic NW and the excitonic and vibrational modes of an organic coating layer, discovering stronger coupling between dark antenna modes and the molecular excitons. This research is extended to multiple different geometries by Kordahl and Dwyer [221], who confirm that coupling with adsorbed molecules can be detected even when the electron beam is on the far side of

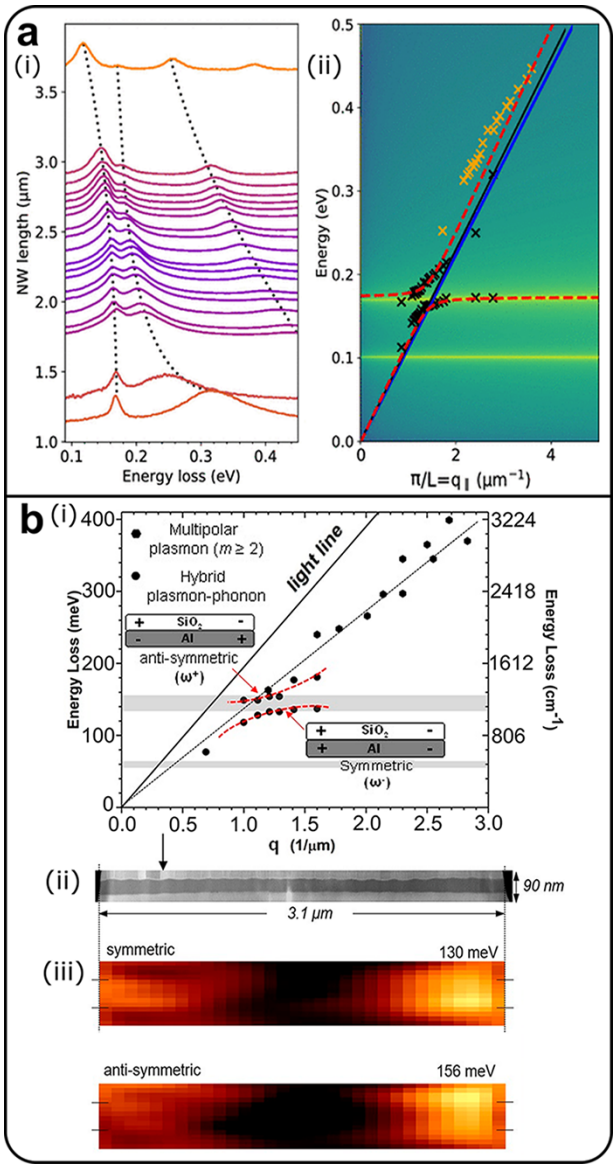

Fig. 13. Strong coupling in plasmon–phonon systems. (a) (i) Experimental EELS spectra of a silver NW with varying length coupling to vibrational modes in *h*-BN; (ii) theoretical dispersion of the interaction between the silver NW dipole and *h*-BN, demonstrating strong coupling as observed by the avoided crossing behaviour. (Adapted with permission from [220]. © 2020 American Chemical Society.) (b) (i) Dispersion curve of coupled SiO_2/Al antenna system, with anti-crossing behaviour of the antenna dipoles observed in the SiO_2 RB; (ii) ADF-STEM image of the coupled antenna system and (iii) EELS scattering maps of the symmetric and anti-symmetric coupled modes. (Adapted with permission from [144]. © 2021 American Chemical Society.)

the metallic nanoparticle and the weak signal from molecular vibrations can be enhanced by several thousand times through coupling with resonant LSPR fields. This opens up new possibilities for extremely remote sensing of coupled excitations, thereby avoiding damage of beam-sensitive organic molecules.

Concluding remarks

The research area of EELS for very low energy excitations (phonons, IR plasmons and strongly coupled modes) has grown rapidly very recently, enabled by remarkable advancements in monochromator technology. The examples reviewed above show experimental results spanning spectral ranges from the MIR to the UV in a large variety of nanoscale materials, with ongoing studies yet to reveal more exciting discoveries.

In the arena of vibEELS, numerous reports illustrate the astounding capabilities of spatially resolved EELS for the study of vibrational properties with high spatial and spectral sensitivity, in both real and momentum space. The basic understanding of inelastic electron scattering from lattice phonons in solids has progressed due to the development of theoretical models accounting for complex processes associated with the scattering of relativistic electrons in crystals. However, the development of realistic models accounting for atom-sized structural features is still in its early stages. Those new models should provide physical insights into the coupling between a fast electron and an individual vibrational mode,

going beyond the current state of qualitative comparisons between EEL spectra and the phonon DOS. Additional experiments under different illumination and collection conditions can be designed to extend our understanding of scattering signal. Efforts on both theoretical and experimental fronts continue to propel the field, leading to the use of vibEELS as an advanced characterization method for nanomaterials, equivalent in benefit to analytical tools such as core-loss EELS.

Current energy resolution improvements have allowed the detection of optical phonon polaritons in individual nanostructures within narrow energy (reststrahlen) bands. Further instrumental improvements will reveal richer spectral data containing finer details, as typically encountered in optical spectral data. Moreover, electron probes provide access to modes that are inaccessible with other traditional far-field probes (e.g. dark polaritons), thus allowing the identification of new channels for energy-transfer processes associated with light–matter interaction. Future spatially resolved EELS studies on terahertz materials with high anisotropy and exotic configurations and at different temperatures will require the extension of traditional dielectric models to describe their phonon polariton response.

Significant work on the excitation of molecular vibrational modes and interactions between molecules has already been performed by the IR spectroscopy community; the vibEELS community must capitalize and build on these existing foundations of knowledge. Electron beams hold the promise of being able to access optically inactive modes with extremely high spatial sensitivity compared to traditional far-field infrared techniques. However, challenges still remain in the study of complex biological structures such as proteins, as theoreticians tackle challenges associated with the description of inelastic electron scattering from non-periodic atomic arrangements, and experimentalists face the challenges of preparing pristine samples and realizing damage-free spectroscopy under different temperature conditions.

In the context of plasmonics, recent progress reflects the needs of applications in pushing the plasmonic response to ever lower IR energies, while controlling the LSPR behaviour and damping properties. EELS studies in metal-based plasmonics provide valuable information on corner, edge and cavity LSPR modes and how these modes interact with structural defects or couple across nanogaps. For example, the underpinnings of broadband plasmonic responses have been studied deeply with EELS in random and controlled fractal structures. Although EELS probes both light and dark LSPR modes with nanoscale spatial resolution, use of the localized probe also means that EELS is blind to the plasmon phase and researchers must develop new and innovative strategies to overcome this limitation (e.g. beam-shaping, ptychography or phase-retrieval electron microscopy methods).

The plasmonic community's desire to reduce damping, increase the confinement factor and produce active, switchable plasmonic devices across a broad spectral range inspires the EELS community to study plasmonic behaviour in semiconducting materials. With the more complex band structure and electronic response intrinsic to semiconductors, there are several competing factors affecting their plasmonic response. EELS studies highlight that there is more to account for than simply the dopant concentration, including the effects of crystalline defects, such as grain boundaries, or inhomogeneous doping. Initial studies on these materials have begun, but electron microscopy still has an important role in unravelling the numerous factors at play in a whole slew of new materials and active dopants.

We can now probe the dephasing time and quality factor of the plasmon peaks, retrieving information on how the use of different materials or the presence of defects affects plasmon lifetime in different spectral ranges. EELS studies on plasmonic nanostructures must soon turn towards providing the fundamental physics for the intelligent engineering of plasmonic responses for specific applications. As plasmonic device applications continue to grow, the EELS community must continue to push experimental techniques beyond acquiring low-loss maps, into probing the responses of active plasmonic devices under external stimuli, such as temperature, voltage and optical excitation, or in liquid environments.

The field of strong coupling between plasmons and other harmonic excitations is relatively new to electron microscopy. Despite this, the EELS community has quickly seized on the background provided by years of optical studies and has already demonstrated strong coupling in plasmon–exciton and plasmon–phonon systems, mapping out the dispersion relationships of the hybrid modes. EELS has also revealed that strong coupling can occur with optically dark modes, and theoretical calculations reveal that there may be interesting dynamics at play regarding near-field vs far-field responses. Initial theoretical studies also predict coupling of plasmonic modes with molecular vibrational harmonics, proposing a new ultra-aloof way to detect these vibrations in beam-sensitive organic molecules. The combination of highly monochromated electron beams and extremely sensitive direct detectors provides the environment needed for electron spectroscopists to experimentally validate these theoretical predictions.

Spatially resolved imaging techniques for probing low-energy excitations in real and reciprocal space are essential tools for understanding and describing their physical behaviour. Angle-resolved scattering maps can now be obtained using 10 meV and 1–2-nm-wide electron probes, allowing the study of phonon and plasmon behaviour, including electronic structure, in nanoscale systems with unmatched spatial resolution. Additional technological improvements in the stability and performance of monochromators, spectrometers and *in situ* holders currently underway will provide further opportunities for exploring this rich field of excitations.

Overall, the many findings reported above represent the first steps on the quest to gain an in-depth understanding of IR material properties using electron beam spectroscopy, leaving many exciting new discoveries to be made in various research areas (e.g. heat transfer, quantum materials, infrared photonics, biomaterials and active plasmonics) in the near future.

Funding

The authors acknowledge financial support from the Discovery Grant program and the Natural Sciences and Engineering Research Council of Canada.

Conflicts of Interest

The authors have no known conflicts of interest to declare.

Acknowledgement

We are grateful to Ray Egerton, Philip Batson and Microscopy reviewers for conducting a thorough revision of this review paper. We also thank Tracy Lovejoy, Niklas Dellby and Ondrej Krivanek for providing the 3.7 meV energy resolution spectrum (Fig. 1b) obtained with the CCEM Nion microscope. We thank Victoria Martinez for helping with acquiring copyright permissions to reproduce figures from other works.

References

1. Batson P E, Dellby N, and Krivanek O L (2002) Sub-å ngstrom resolution using aberration corrected electron optics. *Nature* 418: 617–620.
2. Haider M, Uhlemann S, Schwan E, Rose H, Kabius B, and Urban K (1998) Electron microscopy image enhanced. *Nature* 392: 768–769.
3. Brown L M, Batson P E, Dellby N, and Krivanek O L (2015) Brief history of the Cambridge STEM aberration correction project and its progeny. *Ultramicroscopy* 157: 88–90.
4. Urban K W (2015) In quest of perfection in electron optics: A biographical sketch of Harald Rose on the occasion of his 80th birthday. *Ultramicroscopy* 151: 2–10.
5. Hawkes P W (2015) The correction of electron lens aberrations. *Ultramicroscopy* 156: A1–A64.
6. Smith D J (2008) Development of aberration-corrected electron microscopy. *Microsc. Microanal.* 14: 2–15.
7. Krivanek O L, Dellby N, and Murfitt M F (2009) Aberration Correction in Electron Microscopy. *Handbook of Charged Particle Optics*, Second edition, (CRC Press).
8. Chen Z, Jiang Y, Shao Y-T, Holtz M E, Odstrčil M, Guizar-Sicairos M, Hanke I, Ganschow S, Schlom D G, and Muller D A (2021) Electron ptychography achieves atomic-resolution limits set by lattice vibrations. *Science* 372: 826–831.
9. Jiang Y, Chen Z, Han Y, Deb P, Gao H, Xie S, Purohit P, Tate M W, Park J, Gruner S M, Elser V, and Muller D A (2018) Electron ptychography of 2D materials to deep sub-angström resolution. *Nature* 559: 343–349.
10. Suenaga K, Tencé M, Mory C, Colliex C, Kato H, Okazaki T, Shinohara H, Hirahara K, Bandow S, and Iijima S (2000) Element-Selective single atom imaging. *Science* 290: 2280–2282.
11. Gloter A, Badjeck V, Bocher L, Brun N, March K, Marinova M, Tencé M, Walls M, Zobelli A, Stéphan O, and Colliex C (2017) Atomically resolved mapping of EELS fine structures. *Mater. Sci. Semicond. Process.* 65: 2–17.
12. Krivanek O L, Dellby N, Hachtel J A, Idrobo J C, Hotz M T, Plotkin-Swing B, Bacon N J, Bleloch A L, Corbin G J, Hoffman M V, Meyer C E, and Lovejoy T C (2019) Progress in ultrahigh energy resolution EELS. *Ultramicroscopy* 203: 60–67.
13. Faruqi A R, and McMullan G (2018) Direct imaging detectors for electron microscopy. *Nucl. Instrum. Methods Phys. Res. Sect. A* 878: 180–190.
14. Ibach H, and Mills D L (1982). *Electron Energy Loss Spectroscopy and Surface Vibrations*, First edition (Academic Press).
15. Schröder B, and Geiger J (1972) Electron-spectrometric study of amorphous germanium and silicon in the two-phonon region. *Phys. Rev. Lett.* 28: 301–303.
16. Tiemeijer P C (1999) Operation Modes of a TEM Monochromator. *Inst. Phys. Conf. Ser. 161 of Institute of Physics Conference Series*, pp 191–194 (IOP Publishing Ltd, Sheffield).
17. Tiemeijer P C, Lin J H A V, Freitag B H, and Jong A F D (2002) Monochromized 200kV (S)TEM. *Microsc. Microanal.* 8: 70–71.
18. Mukai M, Kim J S, Omoto K, Sawada H, Kimura A, Ikeda A, Zhou J, Kaneyama T, Young N P, Warner J H, Nellist P D, and Kirkland A I (2014) The development of a 200kV monochromated field emission electron source. *Ultramicroscopy* 140: 37–43.
19. Rose H (1999) Prospects for realizing a sub-Å sub-eV resolution EFTEM. *Ultramicroscopy* 78: 13–25.
20. Essers E, Benner G, Mandler T, Meyer S, Mittmann D, Schnell M, and Höschen R (2010) Energy resolution of an Omega-type monochromator and imaging properties of the MANDOLINE filter. *Ultramicroscopy* 110: 971–980.
21. Krivanek O L, Ursin J P, Bacon N J, Corbin G J, Dellby N, Hrncirik P, Murfitt M F, Own C S, and Szilagyi Z S (2009) High-energy-resolution monochromator for aberration-corrected scanning transmission electron microscopy/electron energy-loss spectroscopy. *Philos. Trans. R. Soc. London, Ser. A* 367: 3683–3697.
22. Krivanek O L, Lovejoy T C, Dellby N, and Carpenter R (2013) Monochromated STEM with a 30 meV-wide, atom-sized electron probe. *Microscopy (Tokyo)* 62: 3–21.
23. Kimoto K (2014) Practical aspects of monochromators developed for transmission electron microscopy. *Microscopy (Oxf)* 63: 337–344.
24. Terauchi M, Kuzuo R, Satoh F, Tanaka M, Tsuno K, and Ohyama J (1991) Performance of a new high-resolution electron energy-loss spectroscopy microscope. *Microsc. Microanal. Microstruct.* 2: 351–358.
25. Batson P E, Mook H W and Kruit P (2000) High Brightness Monochromator for STEM. *Inst. Phys. Conf. Ser.*, Vol. 165: pp 213–214 (IOP Publishing Ltd, Hawaii).
26. Terauchi M, Tanaka M, Tsuno K, and Ishida M (1999) Development of a high energy resolution electron energy-loss spectroscopy microscope. *J. Microsc.* 194: 203–209.
27. Krivanek O L, Lovejoy T C, Dellby N, Aoki T, Carpenter R W, Rez P, Soignard E, Zhu J, Batson P E, Lagos M J, Egerton R F, and Crozier P A (2014) Vibrational spectroscopy in the electron microscope. *Nature* 514: 209–212.
28. Rossouw D, and Botton G A (2013) Plasmonic response of bent silver nanowires for nanophotonic subwavelength waveguiding. *Phys. Rev. Lett.* 110: 066801.
29. Miyata T, Fukuyama M, Hibara A, Okunishi E, Mukai M, and Mizoguchi T (2014) Measurement of vibrational spectrum of liquid using monochromated scanning transmission electron microscopy-electron energy loss spectroscopy. *Microscopy* 63: 377–382.
30. Roy D, and Carette J D (1977) Design of Electron Spectrometers for Surface Analysis. H Ibach (ed.), *Electron Spectroscopy for Surface Analysis*, pp 13–58 (Topics in Current Physics, Berlin, Heidelberg: Springer).
31. Kimoto K, Kothleitner G, Grogger W, Matsui Y, and Hofer F (2005) Advantages of a monochromator for bandgap measurements using electron energy-loss spectroscopy. *Micron* 36: 185–189.
32. Politano A (2021) On the Fate of high-resolution electron energy loss spectroscopy (HREELS), a versatile probe to detect surface excitations: will the Phoenix rise again?. *Phys. Chem. Chem. Phys.* 23: 26061–26069.
33. Glauber R J (1955) Time-dependent displacement correlations and inelastic scattering by crystals. *Phys. Rev.* 98: 1692–1698.
34. Van Hove L (1954) Correlations in space and time and born approximation scattering in systems of interacting particles. *Phys. Rev.* 95: 249–262.
35. Earney J J (1971) Phonon scattering of fast electrons by crystals. *Philos. Mag.* 23: 577–583.
36. Rez P (2014) Is localized infrared spectroscopy now possible in the electron microscope?. *Microsc. Microanal.* 20: 671–677.
37. Hohenester U, Trügler A, Batson P E, and Lagos M J (2018) Inelastic vibrational bulk and surface losses of swift electrons in ionic nanostructures. *Phys. Rev. B* 97: 165418.
38. Nicholls R J, Hage F S, McCulloch D G, Ramasse Q M, Refson K, and Yates J R (2019) Theory of momentum-resolved phonon spectroscopy in the electron microscope. *Phys. Rev. B* 99: 094105.

39. Forbes B D, and Allen L J (2016) Modeling energy-loss spectra due to phonon excitation. *Phys. Rev. B* 94: 014110.
40. Dwyer C (2017) Prospects of spatial resolution in vibrational electron energy loss spectroscopy: Implications of dipolar scattering. *Phys. Rev. B* 96: 224102.
41. Niermann T (2019) Scattering of fast electrons by lattice vibrations. *Phys. Rev. B* 100: 144305.
42. Zeiger P M, and Rusz J (2020) Efficient and versatile model for vibrational STEM-EELS. *Phys. Rev. Lett.* 124: 025501.
43. Rez P, and Singh A (2021) Lattice resolution of vibrational modes in the electron microscope. *Ultramicroscopy* 220: 113162.
44. Pines D, and Nozieres P (1999) Massachusetts. *The Theory of Quantum Liquids*, (Perseus Books, USA).
45. Hage F S, Nicholls R J, Yates J R, McCulloch D G, Lovejoy T C, Dellby N, Krivanek O L, Refson K, and Ramasse Q M (2018) Nanoscale momentum-resolved vibrational spectroscopy. *Sci. Adv.* 4: eaar7495.
46. Senga R, Suenaga K, Barone P, Morishita S, Mauri F, and Pichler T (2019) Position and momentum mapping of vibrations in graphene nanostructures. *Nature* 573: 247–250.
47. Egerton R F (2017) Scattering delocalization and radiation damage in STEM-EELS. *Ultramicroscopy* 180: 115–124.
48. Rez P (1993) Does phonon scattering give high-resolution images?. *Ultramicroscopy* 52: 260–266.
49. Lourenço-Martins H, and Kociak M (2017) Vibrational Surface Electron-Energy-Loss Spectroscopy Probes Confined Surface-Phonon Modes. *Phys. Rev. X* 7: 041059.
50. Lagos M J, Trügler A, Amarasinghe V, Feldman L C, Hohenester U, and Batson P E (2018) Excitation of long-wavelength surface optical vibrational modes in films, cubes and film/cube composite system using an atom-sized electron beam. *Microscopy* 67: i3–i13.
51. Venkatraman K, Rez P, March K, and Crozier P A (2018) The influence of surfaces and interfaces on high spatial resolution vibrational EELS from SiO_2. *Microscopy (Oxf)* 67: i14–i23.
52. Konečná A, Venkatraman K, March K, Crozier P A, Hillenbrand R, Rez P, and Aizpurua J (2018) Vibrational electron energy loss spectroscopy in truncated dielectric slabs. *Phys. Rev. B* 98: 205409.
53. Crozier P A (2017) Vibrational and valence aloof beam EELS: A potential tool for nondestructive characterization of nanoparticle surfaces. *Ultramicroscopy* 180: 104–114.
54. Haiber D M, and Crozier P A (2018) Nanoscale probing of local hydrogen heterogeneity in disordered carbon nitrides with vibrational electron energy-loss spectroscopy. *ACS Nano* 12: 5463–5472.
55. Lagos M J, and Batson P E (2018) Thermometry with subnanometer resolution in the electron microscope using the principle of detailed balancing. *Nano Lett.* 18: 4556–4563.
56. Egerton R F (2015) Vibrational-loss EELS and the avoidance of radiation damage. *Ultramicroscopy* 159: 95–100.
57. Ruppin R, and Englman R (1970) Optical phonons of small crystals. *Rep. Prog. Phys.* 33: 149–196.
58. Mills D L, and Burstein E (1974) Polaritons: the electromagnetic modes of media. *Rep. Prog. Phys.* 37: 817–926.
59. Fuchs R, and Kliewer K L (1965) Optical modes of vibration in an ionic crystal slab. *Phys. Rev.* 140: A2076–A2088.
60. Li N, Guo X, Yang X, Qi R, Qiao T, Li Y, Shi R, Li Y, Liu K, Xu Z, Liu L, García de Abajo F J, Dai Q, Wang E-G, and Gao P (2021) Direct observation of highly confined phonon polaritons in suspended monolayer hexagonal boron nitride,. *Nat. Mater.* 20: 43–48.
61. Lagos M J, Trügler A, Hohenester U, and Batson P E (2017) Mapping vibrational surface and bulk modes in a single nanocube. *Nature* 543: 529–532.
62. Chen C H, and Silcox J (1975) Detection of optical surface guided modes in thin graphite films by high-energy electron scattering. *Phys. Rev. Lett.* 35: 389–393.
63. Batson P E, and Lagos M J (2017) Characterization of misfit dislocations in Si quantum well structures enabled by STEM based aberration correction. *Ultramicroscopy* 180: 34–40.
64. Egerton R F, Venkatraman K, March K, and Crozier P A (2020) Properties of dipole-mode vibrational energy losses recorded from a TEM specimen. *Microsc. Microanal.* 26: 1117–1123.
65. Govyadinov A A, Konečná A, Chuvilin A, Vélez S, Dolado I, Nikitin A Y, Lopatin S, Casanova F, Hueso L E, Aizpurua J, and Hillenbrand R (2017) Probing low-energy hyperbolic polaritons in van der Waals crystals with an electron microscope. *Nat. Commun.* 8: 95.
66. Fuchs R (1975) Theory of the optical properties of ionic crystal cubes. *Phys. Rev. B* 11: 1732–1740.
67. Wallis R F (1959) Theory of surface modes of vibration in two- and three-dimensional crystal lattices. *Phys. Rev.* 116: 302–308.
68. Radtke G, Taverna D, Menguy N, Pandolfi S, Courac A, Le Godec Y, Krivanek O L, and Lovejoy T C (2019) Polarization selectivity in vibrational electron-energy-loss spectroscopy. *Phys. Rev. Lett.* 123: 256001.
69. Beutler E K, Lagos M J, and Masiello D J (2021) Infrared surface phonon nanospectroscopy of an interacting dielectric-particle–dielectric-substrate dimer using fast electrons. *Phys. Rev. B* 103: 165418.
70. Qi R, Wang R, Li Y, Sun Y, Chen S, Han B, Li N, Zhang Q, Liu X, Yu D, and Gao P (2019) Probing far-infrared surface phonon polaritons in semiconductor nanostructures at nanoscale. *Nano Lett.* 19: 5070–5076.
71. Leapman R D, Fejes P L, and Silcox J (1983) Orientation dependence of core edges from anisotropic materials determined by inelastic scattering of fast electrons. *Phys. Rev. B* 28: 2361–2373.
72. Qi R, Li N, Du J, Shi R, Huang Y, Yang X, Liu L, Xu Z, Dai Q, Yu D, and Gao P (2021) Four-dimensional vibrational spectroscopy for nanoscale mapping of phonon dispersion in BN nanotubes. *Nat. Commun.* 12: 1179.
73. Plotkin-Swing B, Corbin G J, De Carlo S, Dellby N, Hoermann C, Hoffman M V, Lovejoy T C, Meyer C E, Mittelberger A, Pantelic R, Piazza L, and Krivanek O L (2020) Hybrid pixel direct detector for electron energy loss spectroscopy. *Ultramicroscopy* 217: 113067.
74. Dwyer C, Aoki T, Rez P, Chang S L Y, Lovejoy T C, and Krivanek O L (2016) Electron-Beam Mapping of Vibrational Modes with Nanometer Spatial Resolution. *Phys. Rev. Lett.* 117: 256101.
75. Hage F S, Kepaptsoglou D M, Ramasse Q M, and Allen L J (2019) Phonon spectroscopy at atomic resolution. *Phys. Rev. Lett.* 122: 016103.
76. Batson P E and Silcox J (May), 1983 Experimental energy-loss function, $\mathrm{Im}[-\frac{1}{\epsilon}(q,\omega)]$, for aluminum, *Phys. Rev. B*, 27.
77. Venkatraman K, Levin B D A, March K, Rez P, and Crozier P A (2019) Vibrational spectroscopy at atomic resolution with electron impact scattering. *Nat. Phys.* 15: 1237–1241.
78. Barker A S, and Sievers A J (1975) Optical studies of the vibrational properties of disordered solids. *Rev. Mod. Phys.* 47: S1–S179.
79. Yan X, Liu C, Gadre C A, Gu L, Aoki T, Lovejoy T C, Dellby N, Krivanek O L, Schlom D G, Wu R, and Pan X (2021) Single-defect phonons imaged by electron microscopy. *Nature* 589: 65–69.
80. Zeiger P M, and Rusz J (2021) Simulations of spatially and angle-resolved vibrational electron energy loss spectroscopy for a system with a planar defect. *Phys. Rev. B* 104: 094103.
81. Hage F S, Radtke G, Kepaptsoglou D M, Lazzeri M, and Ramasse Q M (2020) Single-atom vibrational spectroscopy in the scanning transmission electron microscope. *Science* 367: 1124–1127.
82. Wallis R F, Mills D L, and Maradudin A (1968). *Localized Excitations in Solids*, (Plenum Press, New York).
83. Dwyer C (2014) Localization of high-energy electron scattering from atomic vibrations. *Phys. Rev. B* 89: 054103.

84. Saavedra J R M, and García de Abajo F J (2015) Phonon excitation by electron beams in nanographenes. *Phys. Rev. B* 92: 115449.
85. Konečná A, Iyikanat F, and García de Abajo F J (2021) Theory of atomic-scale vibrational mapping and isotope identification with electron beams. *ACS Nano* 15: 9890–9899.
86. Rez P, Aoki T, March K, Gur D, Krivanek O L, Dellby N, Lovejoy T C, Wolf S G, and Cohen H (2016) Damage-free vibrational spectroscopy of biological materials in the electron microscope. *Nat. Commun.* 7: 10945.
87. March K, Venkatraman K, Truong C D, Williams D, Chiu P-L, and Rez P (2021) Protein secondary structure signatures from energy loss spectra recorded in the electron microscope. *J. Microsc.* 282: 215–223.
88. Hachtel J A, Huang J, Popovs I, Jansone-Popova S, Keum J K, Jakowski J, Lovejoy T C, Dellby N, Krivanek O L, and Idrobo J C (2019) Identification of site-specific isotopic labels by vibrational spectroscopy in the electron microscope. *Science* 8: 525–528.
89. Jokisaari J R, Hachtel J A, Hu X, Mukherjee A, Wang C, Konečná A, Lovejoy T C, Dellby N, Aizpurua J, Krivanek O L, Idrobo J-C, and Klie R F (2018) Vibrational Spectroscopy of Water with High Spatial Resolution. *Adv. Mater.* 30: 1802702.
90. Crozier P A, Aoki T, and Liu Q (2016) Detection of water and its derivatives on individual nanoparticles using vibrational electron energy-loss spectroscopy. *Ultramicroscopy* 169: 30–36.
91. Collins S M, Kepaptsoglou D M, Hou J, Ashling C W, Radtke G, Bennett T D, Midgley P A, and Ramasse Q M (2020) Functional group mapping by electron beam vibrational spectroscopy from nanoscale volumes. *Nano Lett.* 20: 1272–1279.
92. Batson P E, and Lagos M J (2018) Interpretation of meV Resolution Phonon EELS Data. *Microsc. Microanal.* 24: 412–413.
93. Boersch H, Geiger J, and Stickel W (1966) Interaction of 25-keV electrons with lattice vibrations in lif. experimental evidence for surface modes of lattice vibration. *Phys. Rev. Lett.* 17: 379–381.
94. Idrobo J C, Lupini A R, Feng T, Unocic R R, Walden F S, Gardiner D S, Lovejoy T C, Dellby N, Pantelides S T, and Krivanek O L (2018) Temperature measurement by a nanoscale electron probe using energy gain and loss spectroscopy. *Phys. Rev. Lett.* 120: 095901.
95. Yan X, Liu C, Gadre C A, Dai S, Gu L, Yu K, Aoki T, Wu R, and Pan X (2019) Unexpected strong thermally induced phonon energy shift for mapping local temperature. *Nano Lett.* 19: 7494–7502.
96. Li X, Haberfehlner G, Hohenester U, Stéphan O, Kothleitner G, and Kociak M (2021) Three-dimensional vectorial imaging of surface phonon polaritons. *Science* 371: 1364–1367.
97. Davis T J, and Gómez D E (2017) Colloquium: An algebraic model of localized surface plasmons and their interactions. *Rev. Mod. Phys.* 89: 011003.
98. García de Abajo F J, and Kociak M (2008) Probing the photonic local density of states with electron energy loss spectroscopy. *Phys. Rev. Lett.* 100: 106804.
99. Hohenester U, Ditlbacher H, and Krenn J R (2009) Electron-Energy-Loss spectra of plasmonic nanoparticles. *Phys. Rev. Lett.* 103: 106801.
100. Bohm D, and Pines D (1951) A Collective Description of Electron Interactions. I. Magnetic Interactions. *Phys. Rev.* 82: 625–634.
101. Pines D, and Bohm D (1952) A Collective Description of Electron Interactions: II. Collective vs Individual Particle Aspects of the Interactions. *Phys. Rev.* 85: 338–353.
102. Bohm D, and Pines D (1953) A Collective Description of-Electron Interactions: III. Coulomb Interactions in a Degenerate Electron Gas. *Phys. Rev.* 92: 609–625.
103. Ritchie R H (1957) Plasma losses by fast electrons in thin films. *Phys. Rev.* 106: 874–881.
104. Powell C J, and Swan J B (1959) Origin of the characteristic electron energy losses in aluminum. *Phys. Rev.* 115: 869–875.
105. Fujimoto F, and Komaki K (1968) Plasma oscillations excited by a fast electron in a metallic particle. *J. Phys. Soc. Jpn.* 25: 1679–1687.
106. Petersen H (1977) Plasma oscillations in oxide free Al clusters. *Solid State Commun.* 23: 931–933.
107. Pettit R B, Silcox J, and Vincent R (1975) Measurement of surface-plasmon dispersion in oxidized aluminum films. *Phys. Rev. B* 11: 3116–3123.
108. Batson P E (1982) Surface plasmon coupling in clusters of small spheres. *Phys. Rev. Lett.* 49: 936–940.
109. Batson P E (1985) Inelastic scattering of fast electrons in clusters of small spheres. *Surf. Sci.* 156: 720–734.
110. Batson P E (1982) A new surface plasmon resonance in clusters of small aluminum spheres. *Ultramicroscopy* 9: 277–282.
111. Achèche M, Colliex C, Kohl H, Nourtier A, and Trebbia P (1986) Theoretical and experimental study of plasmon excitations in small metallic spheres. *Ultramicroscopy* 20: 99–105.
112. Ugarte D, Colliex C, and Trebbia P (1992) Surface- and interface-plasmon modes on small semiconducting spheres. *Phys. Rev. B* 45: 4332–4343.
113. Nelayah J, Kociak M, Stéphan O, García de Abajo F J, Tencé M, Henrard L, Taverna D, Pastoriza-Santos I, Liz-Marzán L M, and Colliex C (2007) Mapping surface plasmons on a single metallic nanoparticle. *Nat. Phys.* 3: 348–353.
114. Rossouw D, Couillard M, Vickery J, Kumacheva E, and Botton G A (2011) Multipolar plasmonic resonances in silver nanowire antennas imaged with a subnanometer electron probe. *Nano Lett.* 11: 1499–1504.
115. Nicoletti O, Wubs M, Mortensen N A, Sigle W, van Aken P A, and Midgley P A (2011) Surface plasmon modes of a single silver nanorod: an electron energy loss study. *Opt. Express* 19: 15371.
116. Koenderink A F, Alú A, and Polman A Nanophotonics: Shrinking light-based technology. *Science* 348: 516–521, 2015.
117. Wei H, Pan D, Zhang S, Li Z, Li Q, Liu N, Wang W, and Xu H (2018) Plasmon waveguiding in nanowires. *Chem. Rev.* 118: 2882–2926.
118. Davis T J, Gómez D E, and Roberts A (2017) Plasmonic circuits for manipulating optical information. *Nanophotonics* 6: 543–559.
119. Bibikova O, Haas J, López-Lorente A I, Popov A, Kinnunen M, Meglinski I, and Mizaikoff B (2017) Towards enhanced optical sensor performance: SEIRA and SERS with plasmonic nanostars. *Analyst* 142: 951–958.
120. Pattanayak S, and Jana S K (2018) Controllable aqueous synthesis of near-IR-plasmonic anisotropic gold nanoparticles in the hydrazine concentration assisted: hydrazine-citrate hydrogen-bonded network at room temperature and application in highly sensitive SERS-based detection of Pb (II) species. *Inorg. Nano-Metal Chem.* 48: 535–540.
121. Law S, Podolskiy V, and Wasserman D (2013) Towards nano-scale photonics with micro-scale photons: the opportunities and challenges of mid-infrared plasmonics. *Nanophotonics* 2: 103–130.
122. Zheng Y, Thai T, Reineck P, Qiu L, Guo Y, and Bach U (2013) DNA-directed self-assembly of core-satellite plasmonic nanostructures: A highly sensitive and reproducible near-IR SERS sensor. *Adv. Funct. Mater.* 23: 1519–1526.
123. González-Campuzano R, Saniger J M, and Mendoza D (2017) Plasmonic resonances in hybrid systems of aluminum nanostructured arrays and few layer graphene within the UV-IR spectral range. *Nanotechnology* 28: 465704.
124. Neubrech F, Pucci A, Cornelius T W, Karim S, García-Etxarri A, and Aizpurua J (2008) Resonant plasmonic and vibrational coupling in a tailored nanoantenna for infrared detection. *Phys. Rev. Lett.* 101: 157403.
125. Wang B, Singh S C, Lu H, and Guo C (2020) Design of aluminum bowtie nanoantenna array with geometrical control to tune LSPR from UV to near-IR for optical sensing. *Plasmonics* 15: 609–621.

126. Naldoni A, Riboni F, Guler U, Boltasseva A, Shalaev V M, and Kildishev A V (2016) Solar-powered plasmon-enhanced heterogeneous catalysis. *Nanophotonics* 5: 112–133.
127. Zhou L, Swearer D F, Zhang C, Robatjazi H, Zhao H, Henderson L, Dong L, Christopher P, Carter E A, Nordlander P, and Halas N J (2018) Quantifying hot carrier and thermal contributions in plasmonic photocatalysis. *Science* 362: 69–72.
128. Brongersma M L, Halas N J, and Nordlander P (2015) Plasmon-induced hot carrier science and technology. *Nat. Nanotechnol.* 10: 25–34.
129. Mukherjee S, Libisch F, Large N, Neumann O, Brown L V, Cheng J, Lassiter J B, Carter E A, Nordlander P, and Halas N J (2013) Hot electrons do the impossible: plasmon-induced dissociation of H_2 on Au. *Nano Letters* 13: 240–247.
130. Zhang Y, Manjavacas A, Hogan N J, Zhou L, Ayala-Orozco C, Dong L, Day J K, Nordlander P, and Halas N J (2016) Toward surface plasmon-enhanced optical parametric amplification (SPOPA) with engineered nanoparticles: a nanoscale tunable infrared source. *Nano Lett.* 16: 3373–3378.
131. Wu Y, Li G, and Camden J P (2018) Probing nanoparticle plasmons with electron energy loss spectroscopy. *Chem. Rev.* 118: 2994–3031.
132. García de Abajo F J (2010) Optical excitations in electron microscopy. *Rev. Mod. Phys.* 82: 209–275.
133. Silkin V M, Pitarke J M, Chulkov E V, and Echenique P M (2005) Acoustic surface plasmons in the noble metals Cu, Ag, and Au. *Phys. Rev. B* 72: 115435.
134. Dastmalchi B, Tassin P, Koschny T, and Soukoulis C M (2016) A new perspective on plasmonics: confinement and propagation length of surface plasmons for different materials and geometries. *Adv. Opt. Mater.* 4: 177–184.
135. Bernardi M, Mustafa J, Neaton J B, and Louie S G (2015) Theory and computation of hot carriers generated by surface plasmon polaritons in noble metals. *Nat. Commun.* 6: 1–9.
136. Amendola V, Bakr O M, and Stellacci F (2010) A study of the surface plasmon resonance of silver nanoparticles by the discrete dipole approximation method: effect of shape, size, structure, and assembly. *Plasmonics* 5: 85–97.
137. Koh A L, Bao K, Khan I, Smith W E, Kothleitner G, Nordlander P, Maier S A, and McComb D W (2009) Electron energy-loss spectroscopy (EELS) of surface plasmons in single silver nanoparticles and dimers: Influence of beam damage and mapping of dark modes. *ACS Nano* 3: 3015–3022.
138. Johnson P B, and Christy R (1972) Optical constants of the noble metals. *Phys. Rev. B* 6: 4370.
139. Jiang Y, Pillai S, and Green M A (2016) Realistic silver optical constants for plasmonics. *Sci. Rep.* 6: 1–7.
140. Collins S M, Nicoletti O, Rossouw D, Ostasevicius T, and Midgley P A (2014) Excitation dependent Fano-like interference effects in plasmonic silver nanorods. *Phys. Rev. B* 90: 155419.
141. Konečná A, Neuman T, Aizpurua J, and Hillenbrand R (2018) Surface-Enhanced molecular electron energy loss spectroscopy. *ACS Nano* 12: 4775–4786.
142. Wu Y, Hu Z, Kong X-T, Idrobo J C, Nixon A G, Rack P D, Masiello D J, and Camden J P (2020) Infrared plasmonics: STEM-EELS characterization of Fabry-Pérot resonance damping in gold nanowires. *Phys. Rev. B* 101: 085409.
143. Mkhitaryan V, March K, Tseng E N, Li X, Scarabelli L, Liz-Marzán L M, Chen S-Y, Tizei L H, Stéphan O, and Song J-M (2021) Can copper nanostructures sustain high-quality plasmons? *Nano Lett.* 21: 2444–2452.
144. Lagos M J, Batson P E, Lyu Z, and Hohenester U (2021) Imaging strongly coupled plasmon-phonon modes in mid-infrared double antennas. *ACS Photonics* (May) 8: 1293–1300.
145. Prodan E, Radloff C, Halas N J, and Nordlander P (2003) A hybridization model for the plasmon response of complex nanostructures. *Science* 302: 419–422.
146. Mousavi S S M, Bicket I C, Bellido E P, Soleymani L, and Botton G A (2020) Electron energy-loss spectroscopy of surface plasmon activity in wrinkled gold structures. *J. Chem. Phys.* 153: 224703.
147. Mousavi M. S S, Rosendahl S, Read S and Botton G A (2020) Surface plasmonic properties of wrinkled gold wires and films: An electron energy loss spectroscopy microscopic polarization modulation infrared study. *2020 Photonics North (PN)*, pp 1–1.
148. Wang X, Liu C, Gao C, Yao K, Masouleh S S M, Berté R, Ren H, Menezes L d S, Cortés E, Bicket I C, Wang H, Li N, Zhang Z, Li M, Xie W, Yu Y, Fang Y, Zhang S, Xu H, Vomiero A, Liu Y, Botton G A, Maier S A, and Liang H (2021) Self-Constructed multiple plasmonic hotspots on an individual fractal to amplify broadband hot electron generation,. *ACS Nano* 15: 10553–10564.
149. Forcherio G T, DeJarnette D, Benamara M, and Roper D K (2016) Electron energy loss spectroscopy of surface plasmon resonances on aberrant gold nanostructures. *J. Phys. Chem. C* 120: 24950–24956.
150. Bicket I C, Bellido E P, McRae D M, Lagugné-Labarthet F, and Botton G A (2020) Hierarchical plasmon resonances in fractal structures. *ACS Photonics* 7: 1246–1254.
151. Campos A, Arbouet A, Martin J, Gérard D, Proust J, Plain J, and Kociak M (2017) Plasmonic breathing and edge modes in aluminum nanotriangles. *ACS Photonics* 4: 1257–1263.
152. Bellido E P, Manjavacas A, Zhang Y, Cao Y, Nordlander P, and Botton G A (2016) Electron energy-loss spectroscopy of multipolar edge and cavity modes in silver nanosquares. *ACS Photonics* 3: 428–433.
153. Milagres de Oliveira T, Albrecht W, González-Rubio G, Altantzis T, Lobato Hoyos I P, Béché A, Van Aert S, Guerrero-Martínez A, Liz-Marzán L M, and Bals S (2020) 3D characterization and plasmon mapping of gold nanorods welded by femtosecond laser irradiation. *ACS Nano* 14: 12558–12570.
154. Sergeant N P, Hadipour A, Niesen B, Cheyns D, Heremans P, Peumans P, and Rand B P (2012) Design of transparent anodes for resonant cavity enhanced light harvesting in organic solar cells. *Adv. Mater.* 24: 728–732.
155. Bicket I C, Bellido E P, McRae D M, Lagugné-Labarthet F, and Botton G A (2019) Carving plasmon modes in silver Sierpiński fractals. *ACS Photonics* 6: 2974–2984.
156. Genç A, Patarroyo J, Sancho-Parramon J, Arenal R, Duchamp M, Gonzalez E E, Henrard L, Bastús N G, Dunin-Borkowski R E, and Puntes V F (2016) Tuning the plasmonic response up: hollow cuboid metal nanostructures. *ACS Photonics* 3: 770–779.
157. Paul K K, and Giri P K (2017) Role of surface plasmons and hot electrons on the multi-step photocatalytic decay by defect enriched Ag@ TiO_2 nanorods under visible light. *J. Phys. Chem. C* 121: 20016–20030.
158. Saito H, Lourenço-Martins H, Bonnet N, Li X, Lovejoy T C, Dellby N, Stéphan O, Kociak M, and Tizei L H G (2019) Emergence of point defect states in a plasmonic crystal. *Phys. Rev. B* 100: 245402.
159. Raza S, Stenger N, Pors A, Holmgaard T, Kadkhodazadeh S, Wagner J B, Pedersen K, Wubs M, Bozhevolnyi S I, and Mortensen N A (2014). Extremely confined gap surface-plasmon modes electrons. *Nat. Commun.* excited by. 5: 1–7.
160. Kadkhodazadeh S, de Lasson J R, Beleggia M, Kneipp H, Wagner J B, and Kneipp K (2014) Scaling of the surface plasmon resonance in gold and silver dimers probed by EELS. *J. Phys. Chem. C* 118: 5478–5485.
161. Bellido E P, Zhang Y, Manjavacas A, Nordlander P, and Botton G A (2017) Plasmonic coupling of multipolar edge modes and the formation of gap modes. *ACS Photonics* 4: 1558–1565.
162. Smith K C, Olafsson A, Hu X, Quillin S C, Idrobo J C, Collette R, Rack P D, Camden J P, and Masiello D J (2019) Direct observation of infrared plasmonic fano antiresonances by a nanoscale electron probe. *Phys. Rev. Lett.* 123: 177401.

163. Baumberg J J, Aizpurua J, Mikkelsen M H, and Smith D R (2019) Extreme nanophotonics from ultrathin metallic gaps. *Nat. Mater.* 18: 668–678.
164. Nicoletti O, de la Peña F, Leary R K, Holland D J, Ducati C, and Midgley P A (2013) Three-dimensional imaging of localized surface plasmon resonances of metal nanoparticles. *Nature* 502: 80–84.
165. Collins S M, Ringe E, Duchamp M, Saghi Z, Dunin-Borkowski R E, and Midgley P A (2015) Eigenmode tomography of surface charge oscillations of plasmonic nanoparticles by electron energy loss spectroscopy. *ACS Photonics* 2: 1628–1635.
166. Collins S M, and Midgley P A (2017). Progress and opportunities in EELS and EDS tomography. *Ultramicroscopy* 180: 133–141.
167. Hörl A, Haberfehlner G, Trügler A, Schmidt F-P, Hohenester U, and Kothleitner G (2017) Tomographic imaging of the photonic environment of plasmonic nanoparticles. *Nat. Commun.* 8: 37.
168. Haberfehlner G, Schmidt F-P, Schaffernak G, Hörl A, Trügler A, Hohenau A, Hofer F, Krenn J R, Hohenester U, and Kothleitner G (2017) 3D imaging of gap plasmons in vertically coupled nanoparticles by EELS tomography. *Nano Lett.* 17: 6773–6777.
169. Khamh H, Sachet E, Kelly K, Maria J-P, and Franzen S (2018) As good as gold and better: conducting metal oxide materials for mid-infrared plasmonic applications. *J. Mater. Chem. C* 6: 8326–8342.
170. Naik G V, Shalaev V M, and Boltasseva A (2013) Alternative Plasmonic Materials: Beyond gold and silver. *Adv. Mater.* 25: 3264–3294.
171. Wang Z, Chen C, Wu K, Chong H, and Ye H (2019) Transparent conductive oxides and their applications in near infrared plasmonics. *Phys. Status Solidi A* 216: 1700794.
172. Hsieh W T, Wu P C, Khurgin J B, Tsai D P, Liu N, and Sun G (2018) Comparative analysis of metals and alternative infrared plasmonic materials. *ACS Photonics* 5: 2541–2548.
173. Boltasseva A, and Atwater H A (2011) Low-Loss plasmonic metamaterials. *Science* 331: 290–291.
174. Maier S A (2007) Surface Plasmon Polaritons at Metal/Insulator Interfaces. S A Maier (ed..), *Plasmonics: Fundamentals and Applications*, pp 21–37 (Springer US, New York, NY).
175. Pendry J B, Martín-Moreno L, and Garcia-Vidal F J (2004) Mimicking surface plasmons with structured surfaces. *Science* 305: 847–848.
176. Tang W X, Zhang H C, Ma H F, Jiang W X, and Cui T J (2019) Concept, theory, design, and applications of spoof surface plasmon polaritons at microwave frequencies. *Adv. Opt. Mater.* 7: 1800421.
177. Kriegel I, Scotognella F, and Manna L (2017) Plasmonic doped semiconductor nanocrystals: Properties, fabrication, applications and perspectives. *Phys. Rep.* 674: 1–52.
178. Agrawal A, Cho S H, Zandi O, Ghosh S, Johns R W, and Milliron D J (2018) Localized surface plasmon resonance in semiconductor nanocrystals. *Chem. Rev.* 118: 3121–3207.
179. Bertoni G, Ramasse Q, Brescia R, De Trizio L, De Donato F, and Manna L (2019) Direct quantification of Cu vacancies and spatial localization of surface plasmon resonances in copper phosphide nanocrystals. *ACS Mater. Lett.* 1: 665–670.
180. Yang H, Garfunkel E L, and Batson P E (2020) Probing free carrier plasmons in doped semiconductors using spatially resolved electron energy loss spectroscopy. *Phys. Rev. B* 102: 205427.
181. Politano A, Silkin V M, Nechaev I A, Vitiello M S, Viti L, Aliev Z S, Babanly M B, Chiarello G, Echenique P M, and Chulkov E V (2015) Interplay of Surface and Dirac Plasmons in Topological Insulators: The Case of Bi_2Se_3. *Phys. Rev. Lett.* 115: 216802.
182. Casu A, Genovese A, Manna L, Longo P, Buha J, Botton G A, Lazar S, Kahaly M U, Schwingenschloegl U, Prato M, Li H, Ghosh S, Palazon F, De Donato F, Lentijo Mozo S, Zuddas E, and Falqui A (2016) Cu_2Se and Cu Nanocrystals as Local Sources of Copper in Thermally Activated In Situ Cation Exchange. *ACS Nano* 10: 2406–2414.
183. Willhammar T, Sentosun K, Mourdikoudis S, Goris B, Kurttepeli M, Bercx M, Lamoen D, Partoens B, Pastoriza-Santos I, Pérez-Juste J, Liz-Marzán L M, Bals S, and Van Tendeloo G (2017) Structure and vacancy distribution in copper telluride nanoparticles influence plasmonic activity in the near-infrared. *Nat. Commun.* 8: 14925.
184. Tegg L, Cuskelly D, and Keast V J (2018) Plasmon Responses in the Sodium Tungsten Bronzes. *Plasmonics* 13: 437–444.
185. Tegg L, Cuskelly D, and Keast V J (2018) Bulk scale fabrication of sodium tungsten bronze nanoparticles for applications in plasmonics. *Nanotechnology* 29: 40LT02.
186. Sato Y, Terauchi M, and Adachi K (2012) High energy-resolution electron energy-loss spectroscopy study on the near-infrared scattering mechanism of $Cs_{0.33}WO_3$ crystals and nanoparticles. *J. Appl. Phys.* 112: 074308.
187. Sato Y K, Terauchi M, and Adachi K (2019) Anisotropic plasmons due to carrier electrons in Cs-doped hexagonal WO_3 studied by momentum transfer resolved electron energy-loss spectroscopy. *J. Appl. Phys.* 126: 185107.
188. Machida K, Adachi K, Sato Y K, and Terauchi M (2020) Anisotropic dielectric properties and ensemble inhomogeneity of cesium-doped tungsten oxide nanoparticles studied by electron energy loss spectroscopy. *J. Appl. Phys.* 128: 083108.
189. Kapetanovic V, Bicket I C, Lazar S, Lagos M J, and Botton G A (2020) Tunable Infrared Plasmon Response of Lithographic Sn-doped Indium Oxide Nanostructures. *Adv. Opt. Mater.* 8: 2001024.
190. Cho S H, Roccapriore K M, Dass C K, Ghosh S, Choi J, Noh J, Reimnitz L C, Heo S, Kim K, Xie K, Korgel B A, Li X, Hendrickson J R, Hachtel J A, and Milliron D J (2020) Spectrally tunable infrared plasmonic F, Sn : In_2O_3 nanocrystal cubes. *J. Chem. Phys.* 152: 014709.
191. Cho S H, Ghosh S, Berkson Z J, Hachtel J A, Shi J, Zhao X, Reimnitz L C, Dahlman C J, Ho Y, Yang A, Liu Y, Idrobo J-C, Chmelka B F, and Milliron D J (2019) Syntheses of Colloidal F : In_2O_3 Cubes: Fluorine-Induced Faceting and Infrared Plasmonic Response. *Chem. Mater.* 31: 2661–2676.
192. Agrawal A, Singh A, Yazdi S, Singh A, Ong G K, Bustillo K, Johns R W, Ringe E, and Milliron D J (2017) Resonant Coupling between Molecular Vibrations and Localized Surface Plasmon Resonance of Faceted Metal Oxide Nanocrystals. *Nano Lett.* 17: 2611–2620.
193. Maho A, Comeron Lamela L, Henrist C, Henrard L, Tizei L H G, Kociak M, Stéphan O, Heo S, Milliron D J, Vertruyen B, and Cloots R (2019) Solvothermally-synthesized tin-doped indium oxide plasmonic nanocrystals spray-deposited onto glass as near-infrared electrochromic films. *Sol. Energy Mater. Sol. Cells* 200: 110014.
194. Olafsson A, Busche J A, Araujo J J, Maiti A, Idrobo J C, Gamelin D R, Masiello D J, and Camden J P (2020) Electron Beam Infrared Nano-Ellipsometry of Individual Indium Tin Oxide Nanocrystals. *Nano Lett.* 20: 7987–7994.
195. Yazdi S, Agrawal A, Singh A, Milliron D J, and Ringe E (2018) Impact of Non-Uniform Doping on the Plasmonic Properties of In_2O_3 Nanoparticles: A Study by Electron Energy Loss Spectroscopy. *Microsc. Microanal.* 24: 1684–1685.
196. Granerd C S, Bilden S R, Aarholt T, Yao Y-F, Yang C C, Look D C, Vines L, Johansen K M, and Prytz O (2018) Direct observation of conduction band plasmons and the related Burstein-Moss shift in highly doped semiconductors: A STEM-EELS study of Ga-doped ZnO. *Phys. Rev. B* 98: 115301.
197. Politano A, Lamuta C, and Chiarello G Cutting a Gordian Knot: Dispersion of plasmonic modes in Bi_2Se_3 topological insulator. *Appl. Phys. Lett.* 110: 211601, 2017.
198. Kogar A, Vig S, Thaler A, Wong M H, Xiao Y, Reig-i Plessis D, Cho G Y, Valla T, Pan Z, Schneeloch J, Zhong R, Gu G

D, Hughes T L, MacDougall G J, Chiang T-C, and Abbamonte P (2015) Surface collective modes in the topological insulators Bi_2Se_3 and $Bi_{0.5}Sb_{1.5}Te_{3-x}Se_x$. *Phys. Rev. Lett.* 115: 257402.

199. Moradifar P (2020) *Plasmonic resonances in 2D and 3D nanostructures investigated by monochromated electron energy loss spectroscopy (mono-EELS)*. PhD Thesis. Oct., (Pennsylvania, USA), Oct.The Pennsylvania State University.
200. Moradifar P, Bachu S, Sharifi T, Ajayan P, and Alem N (2019) Structural, Optical and Thermal Behavior investigation of 2D Bi_2Te_3/Sb_2Te_3 in-plane Heterostructures via Aberration Corrected STEM and EELS. *Microsc. Microanal.* 25: 2012–2013.
201. Cha J J, Koski K J, Huang K C Y, Wang K X, Luo W, Kong D, Yu Z, Fan S, Brongersma M L, and Cui Y (2013) Two-Dimensional Chalcogenide Nanoplates as Tunable Metamaterials via Chemical Intercalation. *Nano Lett.* 13: 5913–5918.
202. Zhao M, Bosman M, Danesh M, Zeng M, Song P, Darma Y, Rusydi A, Lin H, Qiu C-W, and Loh K P (2015) Visible Surface Plasmon Modes in Single Bi_2Te_3 Nanoplate. *Nano Lett.* 15: 8331–8335.
203. Yang S, and Crozier P (2021) Study of sodium metal plasmon using electron energy loss spectroscopy. *Microsc. Microanal.* 27: 624–625.
204. Biggins J S, Yazdi S, and Ringe E (2018) Magnesium Nanoparticle Plasmonics. *Nano Lett.* 18: 3752–3758 June.
205. Shekhar P, Pendharker S, Sahasrabudhe H, Vick D, Malac M, Rahman R, and Jacob Z (2018) Extreme ultraviolet plasmonics and Cherenkov radiation in silicon. *Optica* 5: 1590–1596.
206. Manfrinato V R, Camino F E, Stein A, Zhang L, Lu M, Stach E A, and Black C T (2019) Patterning Si at the 1 nm Length Scale with Aberration-Corrected Electron-Beam Lithography: Tuning of Plasmonic Properties by Design. *Adv. Funct. Mater.* 29: 1903429.
207. Borja-Urby R, Paredes-Carrera S P, Viltres-Cobas H, Santiago-Jacinto P, Paraguay-Delgado F, Herrera-Pérez G, Rendón-Vázquez L, Sánchez-Ochoa J C, and Morales-Cruz D (2019) Confined volume plasmon spatial distribution by low-loss EELS on self-assemble bismuth nanoparticles. *J. Electron Spectrosc. Relat. Phenom.* 237: 146891.
208. Wang Y W, Kim J S, Kim G H, and Kim K S (2006) Quantum size effects in the volume plasmon excitation of bismuth nanoparticles investigated by electron energy loss spectroscopy. *Appl. Phys. Lett.* 88: 143106.
209. Jin L, Hong C, Zhang D, Gao P, Rao Y, Wang G, Yang Q, Zhong Z, and Zhang H (2020) Synthesis of yttrium iron garnet/bismuth quantum dot heterostructures with localized plasmon enhanced magneto-optical performance. *J. Mater. Sci. Technol.* 51: 32–39.
210. Törmä P, and Barnes W L (2014) Strong coupling between surface plasmon polaritons and emitters: a review. *Rep. Prog. Phys.* 78: 013901.
211. Skolnick M S, Fisher T A, and Whittaker D M (1998) Strong coupling phenomena in quantum microcavity structures. *Semicond. Sci. Technol.* 13: 645–669 July.
212. Bueno-Alejo C J, Graus J, Arenal R, Lafuente M, Bottega-Pergher B, and Hueso J L (2021) Anisotropic Au-ZnO photocatalyst for the visible-light expanded oxidation of n-hexane. *Catal. Today* 362: 97–103.
213. Bertoni G, Fabbri F, Villani M, Lazzarini L, Turner S, Van Tendeloo G, Calestani D, Gradečak S, Zappettini A, and Salviati G (2016) Nanoscale mapping of plasmon and exciton in ZnO tetrapods coupled with Au nanoparticles. *Sci. Rep.* 6: 19168.
214. Shu G-J, Zhou Y, Kao M-Y, Klingshirn C J, Huang M R S, Huang Y-L, Liang Y, Kuo W C H, and Liou S-C Investigation of the π plasmon and plasmon-exciton coupling in titanium diselenide ($TiSe_2$) by momentum-resolved electron energy loss spectroscopy. *Appl. Phys. Lett.* 114: 202103, 2019.
215. Wei J, Jiang N, Xu J, Bai X, and Liu J (2015) Strong Coupling between ZnO Excitons and Localized Surface Plasmons of Silver Nanoparticles Studied by STEM-EELS. *Nano Lett.* 15: 5926–5931.
216. Yankovich A B, Munkhbat B, Baranov D G, Cuadra J, Olsén E, Lourenço-Martins H, Tizei L H G, Kociak M, Olsson E, and Shegai T (2019) Visualizing Spatial Variations of Plasmon-Exciton Polaritons at the Nanoscale Using Electron Microscopy. *Nano Lett.* 19: 8171–8181.
217. Bitton O, Gupta S N, Houben L, Kvapil M, V Křápek, T Šikola, and Haran G (2020) Vacuum Rabi splitting of a dark plasmonic cavity mode revealed by fast electrons. *Nat. Commun.* 11: 487.
218. Zouros G P, Kolezas G D, Mortensen N A, and Tserkezis C (2020) Monitoring strong coupling in nonlocal plasmonics with electron spectroscopies. *Phys. Rev. B* 101: 085416.
219. Crai A, Demetriadou A, and Hess O (2020) Electron Beam Interrogation and Control of Ultrafast Plexcitonic Dynamics. *ACS Photonics* 7: 401–410.
220. Tizei L H G, Mkhitaryan V, Lourenço-Martins H, Scarabelli L, Watanabe K, Taniguchi T, Tencé M, Blazit J-D, Li X, Gloter A, Zobelli A, Schmidt F-P, Liz-Marzán L M, García de Abajo F J, Stéphan O and Kociak M (2020) *Tailored Nanoscale Plasmon-Enhanced Vibrational Electron Spectroscopy*. 2973–2979 *Nano Lett.*, 20.
221. Kordahl D, and Dwyer C (2019) Enhanced vibrational electron energy-loss spectroscopy of adsorbate molecules. *Phys. Rev. B* 99: 104110.